ΠΑΝΕΠΙΣΤΗΜΙΟ ΚΡΗΤΗΣ
UNIVERSITY OF CRETE

FABRICATION OF HSFL STRUCTURES ON BULK METALLIC AND SEMICONDUCTING MATERIALS WITH ULTRASHORT LASER PULSES

MSc Thesis

by Christina Siogka

Supervisor: Dr. Emmanuel Stratakis

HERAKLION, JULY 2023
Physic Department, University of Crete, 700 13, Heraklion, Greece
IESL FORTH, 700 13, Vassilika Vouton

Acknowledgements

First and foremost, I would like to express my deepest appreciation to my supervisor Dr. Emmanuel Stratakis for the consistent support and guidance and the opportunities he offered me throughout the last year. He truly provided me with many tools and aspirations for my future in experimental physics. I could have never imagined having a better collaboration for my Master thesis.

I would, also, like to express my sincere gratitude to Dr. George Tsibidis for always being present and willing to help and advise me in every theoretical question and issue, that was raised during the time of my thesis.

Furthermore, I would like to thank all the members of ULMNP group, and more especially my colleagues Dr. Stella Maragkaki, Dr. Ioanna Sakellari, Mrs. Matina Vlahou and Mrs. Maria-Christina Velli for being so supportive and helpful in many aspects of my thesis. Their most important contribution was the trust they have shown me.

Besides them, I also wish to thank Mrs. Alexandra Manousaki for the never-ending hours she spent with me, in the SEM clean room, taking pictures for my thesis, while she provided me with the wisest life advices.

Last but not least, I would like to express my deepest gratitude to my family and to all of the lifetime friends, that I made throughout these years, for always supporting me through this journey.

Table of Contents

1. Introduction

a. Motivation

An abundance of nanostructuring applications, among others, arise from bio-imitation. Nature offers a diverse wealth of functional and optimized surfaces filigreed with micro- and nano-patterns, which incorporate properties that are unmatched in today's artificial materials. The study of these biological systems and natural methods and their replication into biomimetic surfaces is, therefore, desirable and has so far contributed in a broad range of innovative bio-inspired applications in engineering. Only to mention a few, these applications include phenomena of adhesion, friction, wear, lubrication, wetting phenomena, self-cleaning, antifouling, antibacterial phenomena, thermoregulation and optics.[1]

In Fig. 1, some of the many studied natural species and the corresponding SEM images of the biological systems are shown, which only focus on the enhanced optical properties they possess. Particularly for the peacock spiders (Fig. 1e-f), it is indicated that they have hairs with 2D nanogratings on microscale 3D convex surfaces, which can yield at least twice the resolving power of a conventional 2D diffraction grating with the same characteristics. These exceptional properties of natural systems can be induced to materials, through laser fabrication of their surfaces and this technique is commonly referred to as biomimetic laser nanostructuring. Apparently, these red-circled straight-line arrays in Fig. 1f are reproducible on the surface of almost all classes of materials when irradiated with ultrashort pulsed laser sources, and their nano-spacing depends on several laser's parameters and material's properties.[1]

Furthermore, as time passes along with the constant evolution and contribution of science and technology, more and more fine surface processings are attained, so that the final modified surfaces gain enhanced functionalized properties compared to initial unpatterned ones, and hence giving rise to new and more innovative applications. Over the last four decades, the fields of nanotechnology and lasers are growing rapidly, introducing even further and more complex ideas and techniques that are proving beneficial for science and industry. Specifically, the state-of-the-art laser surface nanostructuring has become a promising alternative for the modification of the functionalities of, virtually, all the types of materials, i.e. metals, semiconductors and dielectrics, as micro- and nano-patterning on the surface of solid surfaces is achieved. So far, the manufacturing of nanostructured materials has provided a variety of

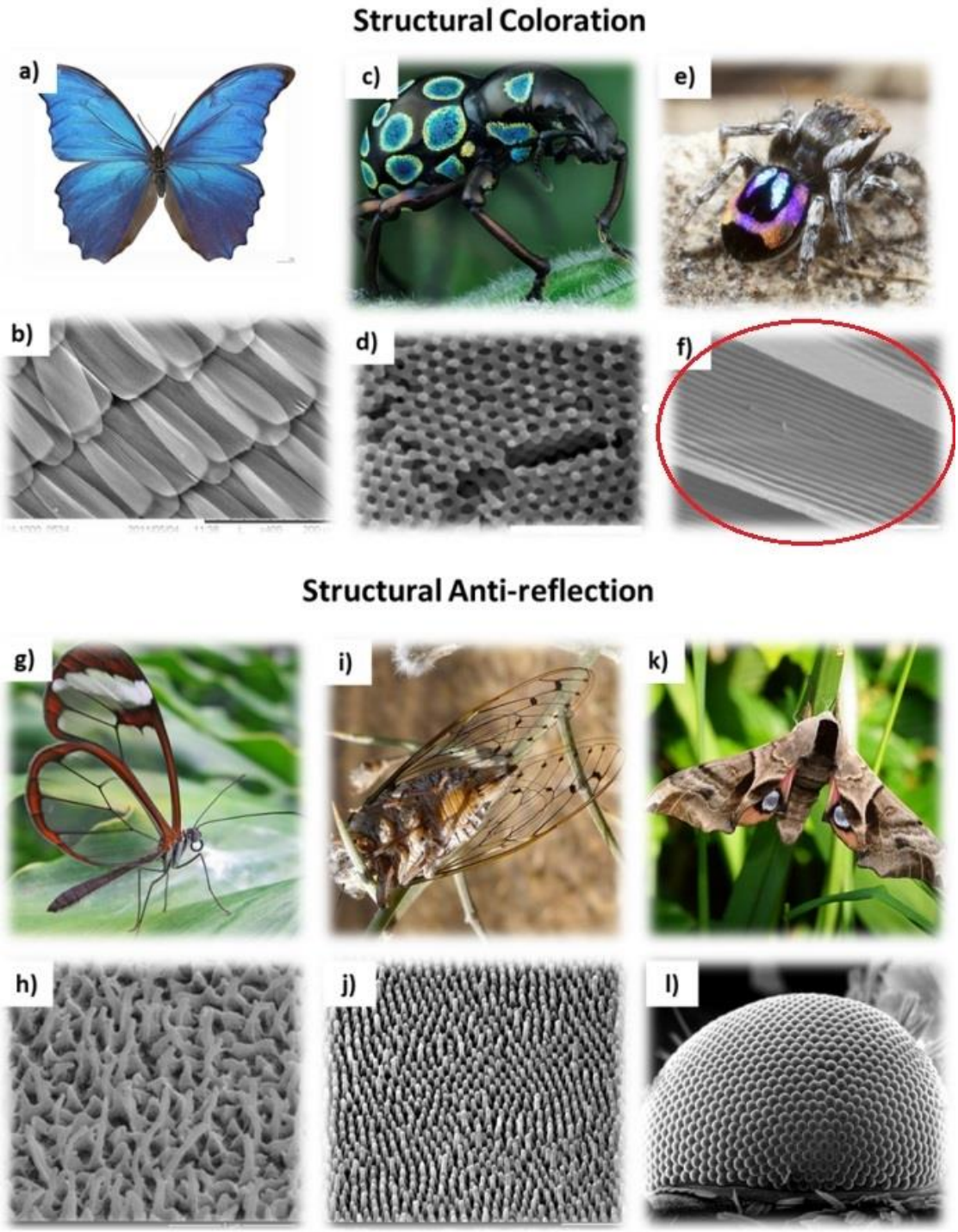

Figure 1. Examples of biological systems with optical properties, photographs of the actual arthropoda and the corresponding SEM image below. The Morpho butterfly with the scales of its wing (a-b), the snout weevil and the ultrastructure of the elytra (i.e. modified forewings) (c-d), as well as the peacock spider and its iridescent scales (e-f) show structural coloration. Structural antireflection was proven for the glasswing butterfly (g-h), a cicada with the nanopillars on its wing (i-j), and the moth's eyes (k-l). Image reproduced from Ref.[1], [36]

applications that have already been integrated in our daily life. In Fig. 2, an overview is shown of the already-identified most relevant applications to date,

of different induced structures and they are arranged into four major groups: photonics, biology/medicine, wetting/microfluidics, as well as other technological applications. However, there is still a plethora of potential innovative technological ideas and benefits, especially for the demanding industrial markets, emerging from this particular technique, i.e. laser surface nanostructuring, and need to be further investigated.[1], [2]

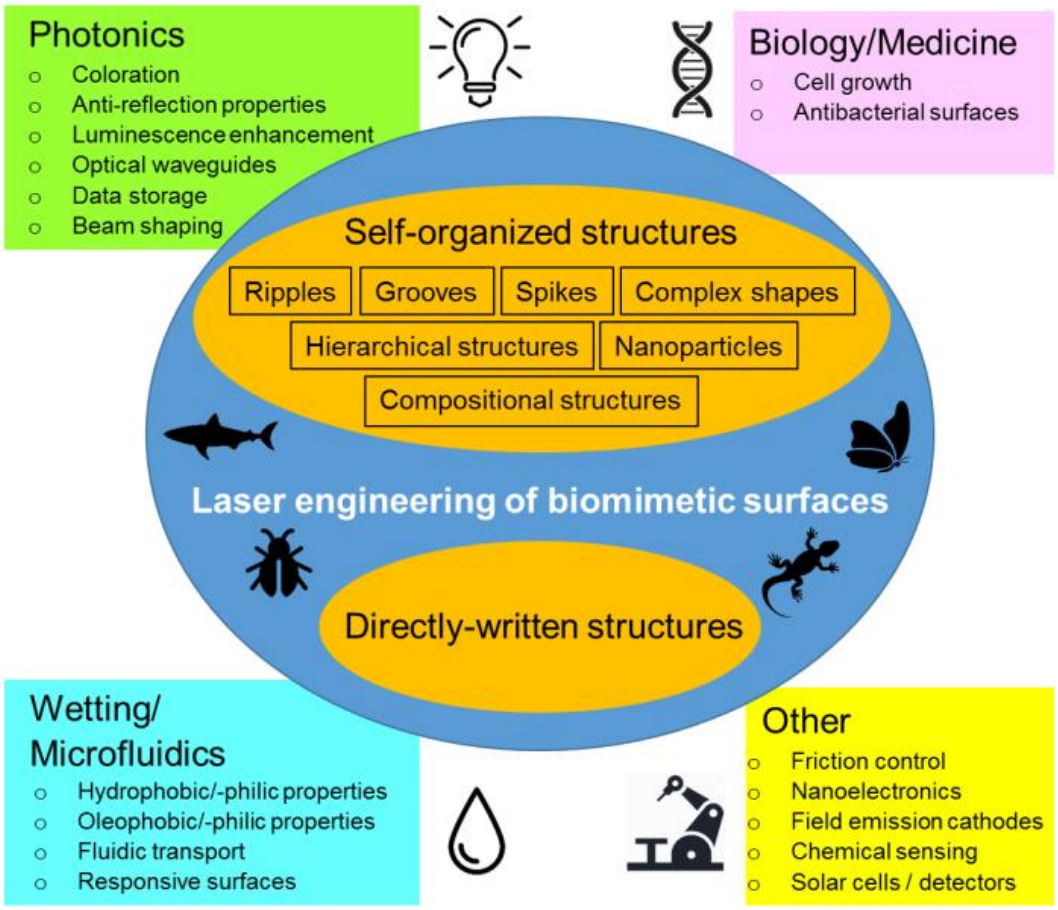

Figure 2. Overview of different applications of laser-fabricated biomimetic surfaces. Image reproduced from Ref. [1]

b. Laser Induced Periodic Surface Structures (LIPSS)

In the early sixties, when the first laser sources were also developed, Milton Birnbaum was the first to report "a regular system of parallel straight lines", that were induced on the surface of a germanium wafer after irradiation with a ruby laser, as seen in Fig. 3. These self-organized periodic surface structures, most commonly called "Laser Induced Periodic Surface Structures (LIPSS)", featured a periodicity of approximately 2 μm, close to the laser wavelength.[3] Since then, extensive research is conducted with the aim to reproduce and to explore the formation mechanism of these structures and to exploit the exotic properties that LIPSS can induce to a solid surface.[2]

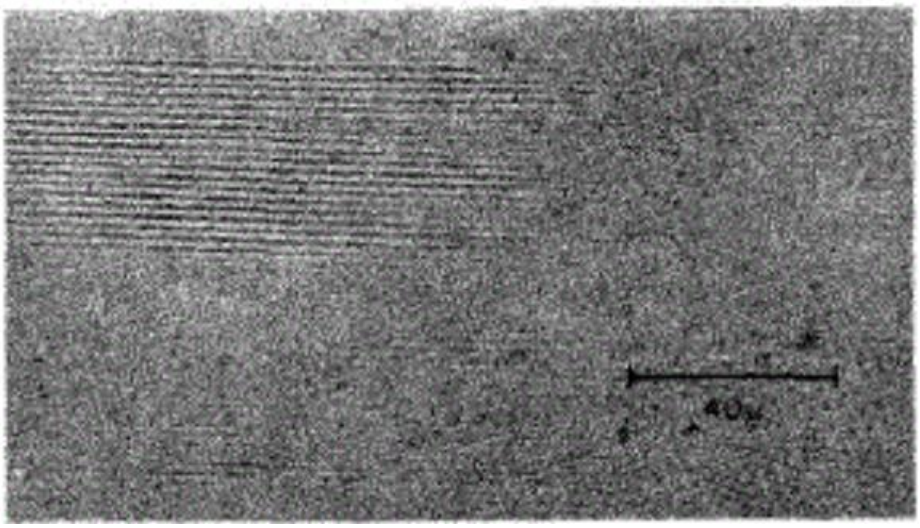

Figure 3. Photomicrograph of surface damage of a (111) face of a germanium sample. Image reproduced from Ref.[3]

To set the foundations of our discussion, LIPSS are a universal phenomenon that can be observed on almost any class of material after its irradiation by ultrashort laser pulses, with durations predominantly in the picosecond to femtosecond range. They are induced structures with periodicities beyond the optical diffraction limit, as they are generated within the focal spot of the laser radiation, and they are wavelength-dependent. Based on their spatial period in relation to the utilized laser wavelength, LIPSS are divided into two groups: Low-Spatial Frequency LIPSS (LSFL) and High-Spatial Frequency LIPSS (HSFL). LSFL feature periods that are larger than half the laser wavelength and can be further sub-classified with respect to their orientation relative to the beam linear polarization direction. On the other hand, HSFL have periods that are smaller than half the laser wavelength and can also be sub-classified according to their depth-to-period aspect ratio.[4] Overall, the spacing of these periodic structures depends both on material's properties, such as the electric permittivity, and on utilized light source's parameters, such as laser wavelength, laser pulse duration, fluence or pulse energy and dose of energy -the number of pulses irradiating the sample, while their orientation depends on the linear polarization state of the laser.

There are many theories that attempt to explain the physical mechanisms behind the formation of LIPSS on the surface of materials. All share one common notion: the surface of the material to be nanostructured needs initially to feature microroughness. On the general case, it is widely accepted, that the formation of LIPSS is attributed to interference of the incident laser beam with the scattered light on the surface. Scattering occurs due to surface's corrugation. This interference results in a spatial redistribution of the beam intensity, because different surface electromagnetic waves are excited, whose

periodicity is finally imprinted on the surface through many mechanisms: ablation, amorphization, and others.[4]

For the case of LSFL, according to most approaches, the ripples are formed due to interference of laser incident light with far-field scattered electromagnetic waves. In the specific case of strong absorbing materials, such as metals, the excitation of Surface Plasmons (SPs) is involved which couple with the incident light and hence the interference results in a periodic modulation of the irradiated surface after the resolidification of the molten material. While the formation of LSFL was sufficiently explained, either on strong absorbing or large bandgap materials, by the theory of interference between the incident laser light and the far-field scattered surface waves, the formation of HSFL is still debatable.[4] Several authors have suggested possible mechanisms, such as a change in refractive index, second harmonic generation (SHG), etc.[5] Apart from these considerations, HSFL in general are assumed to possess such sub-wavelength periodicities due to interference of incident laser light with near-field scattered surface waves, but the mechanism needs to be determined in order to increase the level of control over the laser induced morphology.

The main reason for the employment of LIPSS-based methodology in nano/micro fabrication in the fields of research and industry is the simplicity and robustness of their manufacturing process. Furthermore, laser nanostructuring is a faster, more economic and environmental-friendly technique compared to conventional ones, such as nanolithography. All of these advantages arise in means that permanent surface modifications are attained with the employment of ultrashort laser sources, simple setups and fast translational systems, along with avoiding the necessity of strict environmental conditions like high vacuum or clean rooms or/and the use of toxic chemicals. Thus, the fact that complex surface functionalities can be induced to surfaces with laser nanostructuring, the virtually endless potential of technological ideas along with demanding industries of modern world, proves why they have gained more and more attention and interest over the last years.

To conclude, the topic of this master thesis is to study the evolution of the periodicity of HSFL structures, that are formed on the surface of bulk metals and semiconductors under ultrafast laser irradiation in the near-infrared regime of electromagnetic spectrum, as a function of the peak laser fluence and as a function of the effective number of pulses irradiating the samples. In Section 2, the most useful theoretical considerations For LIPSS are elucidated and proceeding in Section 3, the experimental methods and materials will be described in detail. In Section 4, the results of these studies will be reported and the trend of HSFL periodicity as a function of laser peak and of effective number

of pulses will be attributed to different proposed mechanisms. Finally, in Section 5, the experimental observations and conclusions will be shortly summarized along with some suggestions for further evolvement of HSFL in the future.

2. Theoretical considerations

2.1. Classification of LIPSS

Laser surface structuring can be divided in two different classes: self-organized laser-irradiated structures and direct laser-inscribed structures, as is indicated in Fig. 4. The direct laser inscription, also called micromachining, exploits the laser beam as a tool to modify the surface. However, there is a limitation on the spatial features, on the micrometric scale, of the induced structures, as the spatial resolution is always determined by the laser beam diffraction limit. On the contrary, self-organized surface irradiation results in a characteristic (quasi) periodic modulation of the surface topography in the form of a regular grating and the induced structures have a particular orientation with respect to the linearly polarized laser radiation and are generated within the laser beam spatial limits. Thus, self-organized surface structures are usually further classified as nanometric LIPSS (ripples), and micrometric grooves and spikes, or hybrid variants, as illustrated in Fig. 5.[1]

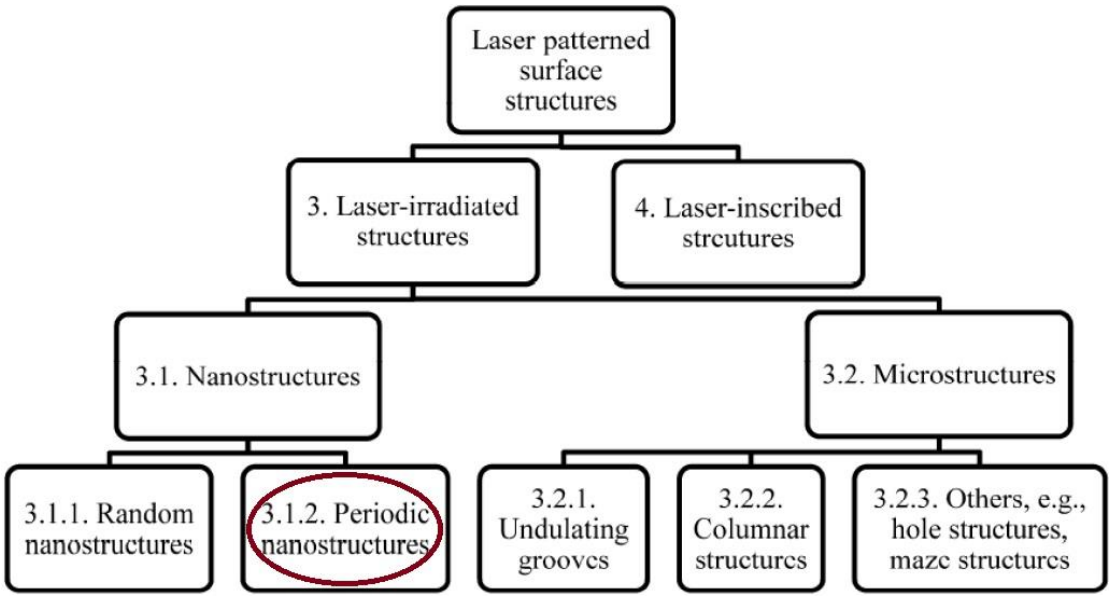

Figure 4. Classification of laser patterned surface structures. Image reproduced from Ref.[1]

LIPSS are observed as High Spatial Frequency LIPSS (HSFL) featuring periods significantly smaller than the irradiation wavelength ($\Lambda < \lambda/2$) or as Low Spatial Frequency LIPSS (LSFL) with periodicities of the order of the laser wavelength ($\Lambda > \lambda/2$)[2], [4], [6] and examples of each type of nanostructures are depicted on Fig. 5 a and b, respectively. As mentioned above, both HSFL and LSFL exhibit a well-defined orientation with respect to a linear polarization state of the

incident laser light. The characteristics such as the periodicity and the orientation of ripples relative to the beam polarization direction, which are both

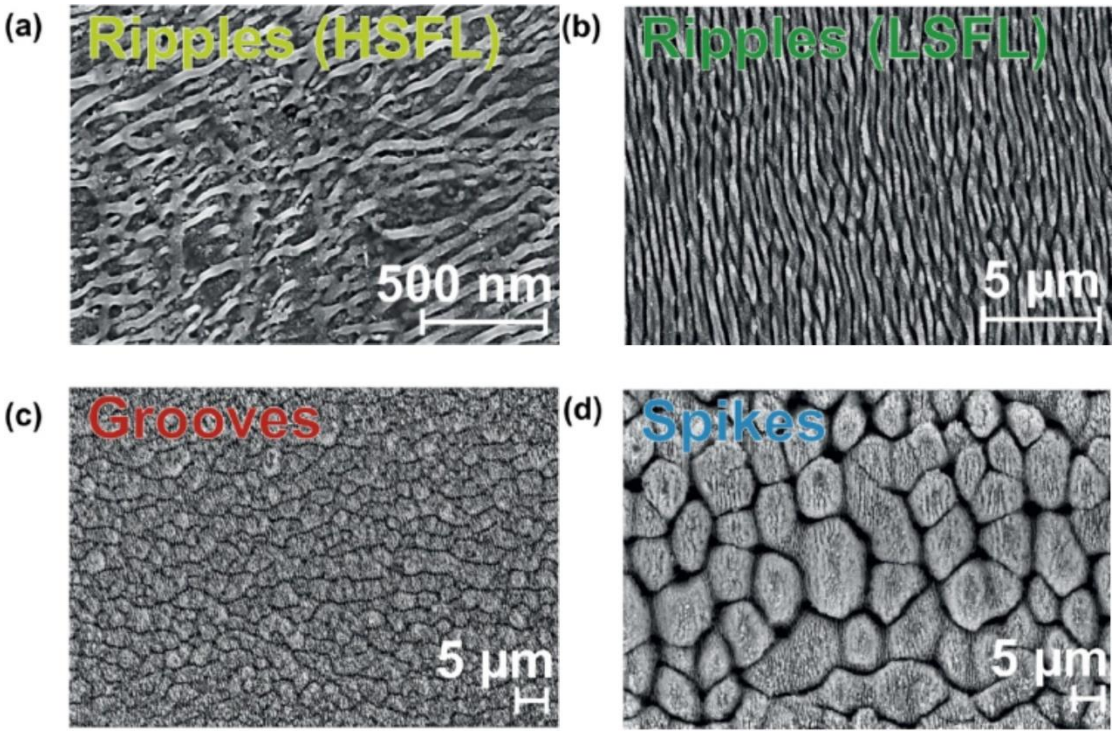

Figure 5. Top-view SEM images of four characteristic surface morphologies observed upon femtosecond laser scan processing of a steel surface [790 nm, 30 fs, 1 kHz]. (a) HSFL, (b) LSFL, (c) Grooves, (d) Spikes. In all cases the linear polarization is horizontal. Note the different magnifications. Image reproduced from Ref.[1]

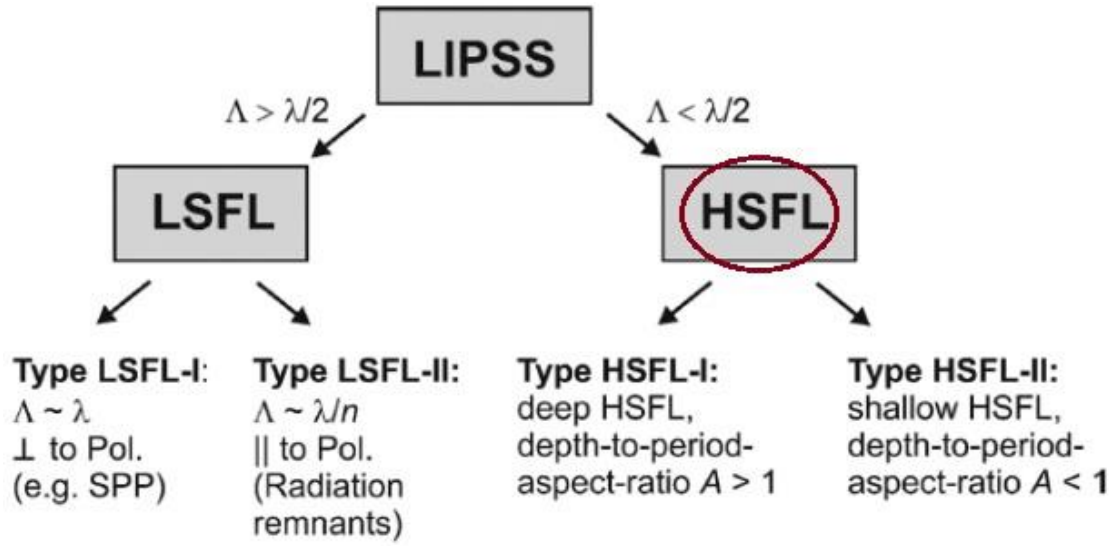

Figure 6. Classification scheme of fs-laser-induced periodic surface structures. Image reproduced from Ref.[1]

determined by the electronic structure of the material and thus by the laser-matter interaction, depend strongly on the type of irradiated material. While on strong absorbing materials, such as metals and semiconductors, LSFL are mainly characterized by $\Lambda \sim \lambda$ and an orientation perpendicular to the laser beam polarization, called LSFL-I, on some large bandgap materials, such as dielectrics, LSFL are generated with $\Lambda \sim \lambda/n$ parallel to beam polarization, called LSFL-II. Here, n refers to the refractive index of the respective dielectric material. On the other hand, HSFL according to the depth-to-period aspect ratio A are classified into the types HSFL-I, with $A > 1$, and HSFL-II, with $A < 1$.[2], [4] These sub-classifications are further clarified in Fig. 6 and in Fig. 7, in which SEM images of the corresponding types of nanostructures are depicted. The emphasis of this thesis will be centered on the formation of HSFL on the surface of bulk metals and semiconductors.

2.2. Physical mechanisms of LIPSS formation – Proposed theoretical models

A thorough investigation of the underlying multiscale phenomena, that take place under irradiation of a solid surface, is required in order to provide a detailed description of the physical origin of LIPSS formation as well as the quantitative features of the induced self-organized structures. Nowadays, the most widely accepted theory suggests that the formation of LIPSS can be attributed to a spatial periodical distribution of the electric field irradiating the solid surface, that transiently transfers to lattice and finally is imprinted on the surface, after the heated material has undergo a phase transition, e.g. melting, and has eventually resolidified.[4] Hopefully, all of these processes take time at different time scales and hence they appear discrete in time, when ultrashort laser pulses are utilized for irradiation of solids, as is the case for the experimental work on this thesis.[7]

When firstly observed by Birnbaum, LIPSS formation was attributed to diffraction effects. In the early seventies, Emmony et al. proposed a mechanism in which the irradiating laser light is scattered on the surface from an existing roughness.[8] They tried to interpret the near-wavelength grating-like surface modification with the interference of the incident electric field with the surface scattered waves excited due to surface corrugation, concluding to the following formula for ripples' periodicity, Λ:

$$\Lambda = \frac{\lambda}{1 \pm \sin\theta} \quad (1)$$

where

- λ is the laser wavelength, and
- θ is the angle of incidence of the laser beam.

For normal incidence, θ = 0, equation (1) gives Λ ~ λ.

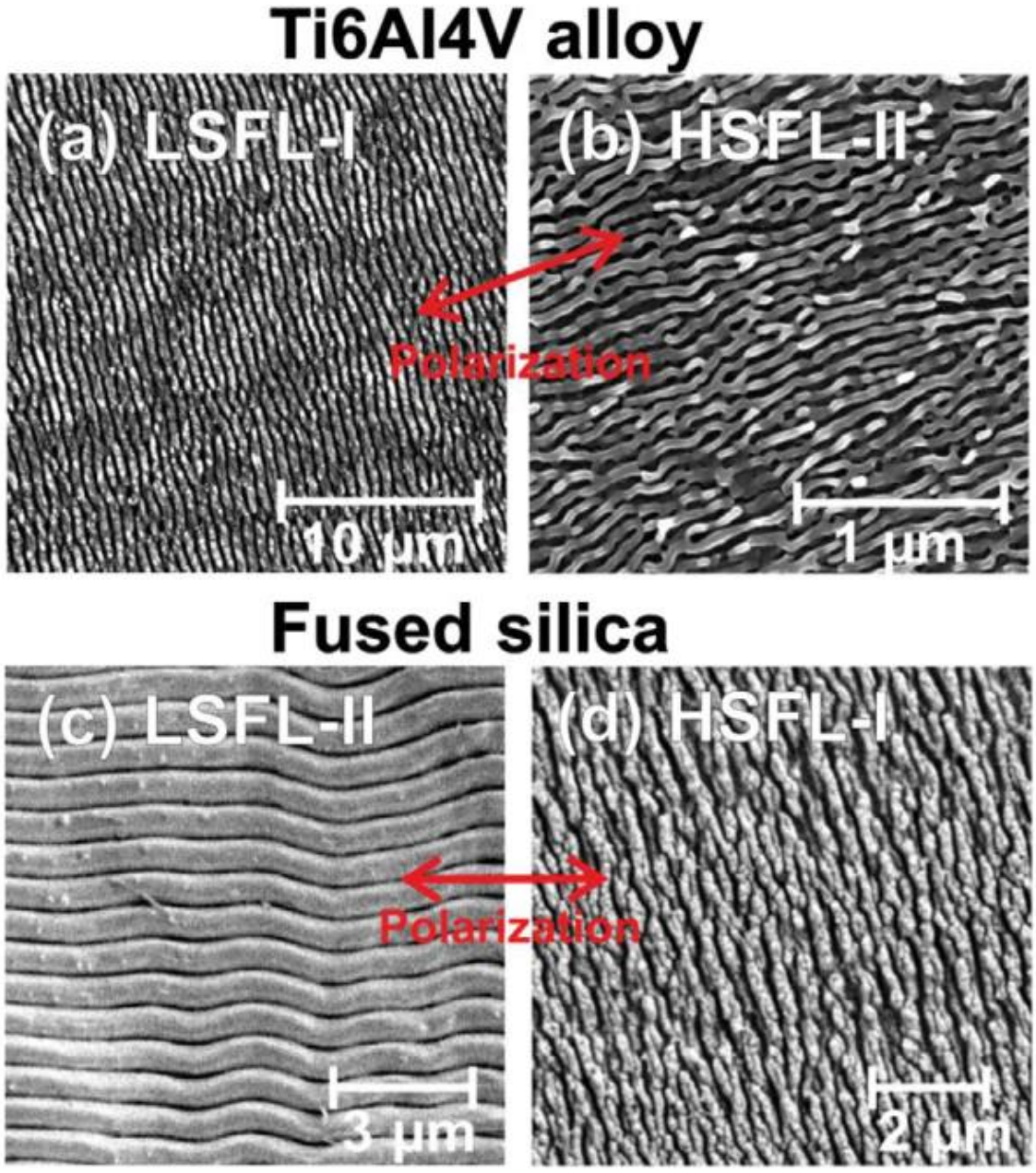

Figure 7. Examples of SEM images of different types of LIPSS (LSFL, HSFL) generated with different fs-laser irradiation conditions on metallic Ti6Al4V titanium alloy (upper row) and on dielectric Fused silica (lower row). (a) LSFL-I, (b) HSFL-II, (c) LSFL-II and (d) HSFL-I. The red double-ended arrows indicate the direction of the linear laser beam polarization. Note the different magnifications of the top-view SEM micrographs. Image reproduced from Ref.[4]

However, in the early eighties, Sipe et. al[9], accounting also for the contribution of polarization direction of the irradiating electric field along with the density of free-excited electrons (carriers), N_e, during irradiation, claimed that the energy deposition on a rough surface is not homogeneous and thus, introduced an efficacy factor, η, which describes the efficacy with which the surface roughness can absorb optical radiation.[4] This factor may exhibit pronounced sharp peaks at specific directions, which can be used to evaluate the associated spatial periods Λ along with the orientation of formed ripples relative to incident laser beam polarization. The formation of ripples was still interpreted with the interference of incident laser light with excited surface electromagnetic modes and Sipe's theory suggests until today a well-established formation mechanism of surface structures. Under specific irradiation conditions these surface scattered waves were attributed to excitation of Surface Plasmons (SPs), which are surface electron density waves, that couple with the incident beam and hence, resulting in Surface Plasmon Polaritons waves (SPPs).[4] SPPs will be thereinafter analyzed in detail, since they are the most prominent LIPSS formation mechanism. After all, by assuming that excitation of SPPs and their interference with incident laser light is responsible for the formation of LIPSS, Sipe's theory predicts possible wavevectors, $\vec{\kappa}$, of the LIPSS, where $|\vec{\kappa}| = \frac{\lambda}{\Lambda}$ is the normalized wavevector, as a function of surface parameters (bulk dielectric permittivity, ε, and surface roughness) and laser irradiation parameters (wavelength, polarization direction, angle of incidence, θ). The inhomogeneous absorption of optical energy by the irradiated material is expressed by:

$$\text{Absorption} \sim \eta(\vec{\kappa}) \times |b(\vec{\kappa})| \tag{2}$$

where

- $\eta(\vec{\kappa})$ describes the enhancement of electric field on irradiated surface, i.e. the efficacy with which a surface roughness at $\vec{\kappa}$ induces inhomogeneous radiation absorption, and
- $b(\vec{\kappa})$ is a measure of the surface roughness at $\vec{\kappa}$.[10]

At last, since the aforementioned approaches do not or fail to account for interference of incident light with the majority of surface scattered waves types -only SPPs are assumed in Sipe's theory- and inter-pulse irradiation, a prior-existing model, called Finite-Difference Time-Domain (FDTD), was employed in order to describe the energy deposition on the surface after multi-pulse irradiation and the excitation of a broad range of different surface

electromagnetic modes.[4] The introduction of this computational method for evaluation of LIPSS periodicities was necessary, since it allows the prediction of a precise spatiotemporal distribution of the energy absorption, which is of great portance at irradiations at large number of pulses in which surface corrugation as well as the modulated profile morphology is expected to influence the amount of deposited energy.[11] In Fig. 8, a direct comparison of analytic Sipe's theory versus numeric FDTD simulation is illustrated, for two reasons: firstly, in order to clarify how particular results can be predicted for the periodicity and the orientation of the laser-induced nanostructures and to point out the differences in results extracted from each method.

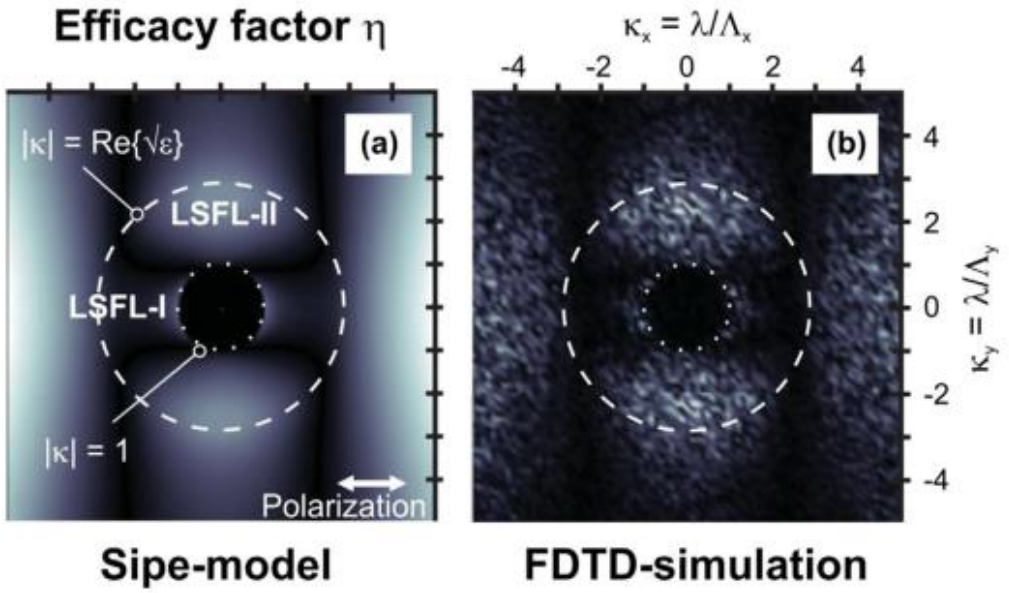

Figure 8. Comparison of the analytic Sipe theory with numeric FDTD-simulations. (a) η (Sipe-model) and (b) FDTD-η maps computed with θ=0, λ = 800 nm. The maps are obtained for weakly laser-excited silicon ($N_e = 2 \times 10^{21}$ cm^{-3}, $\sqrt{\boldsymbol{\varepsilon}} = 2.868 + 0.382i$). The polarization direction is indicated by the white arrow in (a). The dotted and dashed circles represent $|\vec{\boldsymbol{\kappa}}| = 1$ and $|\vec{\boldsymbol{\kappa}}| = \mathrm{Re}(\sqrt{\boldsymbol{\varepsilon}})$, respectively. A linear grayscale color map is used, the brightest areas represent the largest values. The noise in (b) arises from the fact that the FDTD-simulation was performed with a discrete, randomly distributed rough surface. Image reproduced from Ref. [4]

As is evident from Fig. 8, the results obtained with Sipe's theory and FDTD simulation are roughly similar. In principle, LIPSS are observed wherever the efficacy factor exhibits strong variations. By referring to Sipe's model, Fig. 8a, abrupt variations are seen on η, extending perpendicular to laser polarization direction along x-axis at $\kappa_x \sim \pm 1$, indicating an enhancement of electric field on the irradiated surface perpendicular to incident light polarization state and thus, through Fourier Transforms, structures with $\Lambda \sim \lambda$ are predicted to be formed, that are perpendicular to incident beam horizontal polarization. These ripples are of the LSFL-I type, as previously mentioned.[12] Furthermore, similar considerations can be made for the sharp transitions on η, extending parallel to

laser polarization along y-axis at $\kappa_y \sim \pm \mathrm{Re}(\sqrt{\varepsilon})$. This condition indicates the formation of ripples parallel to beam polarization with $\Lambda \sim \lambda/n$, as is the case for LSFL-II. These main predictions of Sipe's theory are validated also from FDTD-simulations in Fig. 8b, but with somewhat different characteristics. As is evident, with FDTD-simulation the areas including the pronounced sharp peaks of efficacy factor are more confined in κ-domain, both along κ_x and κ_y. Therefore, more accurate predictions are to be expected for ripples' periodicity when FDTD-simulation is preferred over the simple Sipe's model.

In the work of Bonse et al.[4], a table including the classification of LIPSS, their origin, orientation with respect to incident laser polarization direction, period, representation in Fourier space and the class of material induced to, summarizes all different types of LIPSS reported up to date in literature and is reproduced in this thesis as well, in Fig. 9. Again, note that LIPSS formation is attributed to interference of incident laser light with surface scattered waves, independently on type. Specifically, HSFL seem to originate from interference of incident light with near-field nonradiative scattering waves.[13] On the following subsections, the excitation of two specific surface electromagnetic modes, SPPs and Second Harmonic Generation (SHG), will be analyzed.

To account for temporal dynamics of LIPSS imprinting on irradiated solid surfaces, the flux of dissipated heat must be considered. One of the most popular theoretical models to predict how heat flows is called Two-Temperature Model (TTM) and is presented qualitatively herein.[1], [14] In general, initially, electron excitation, due to energy absorption, takes place and then heat is transferred from the electron system to the lattice system, through electron-phonon coupling. According to this model, during irradiation with ultrafast laser sources, electrons gain sufficient energy to be excited to conduction band and turn into free carriers. Immediately after excitation, when free electrons are in a highly nonequilibrium state, a fraction of them moves to deeper parts of the material due to ballistic motion, while the others collide with nearby energetic electrons, so that thermal equilibrium within the electronic subsystem is to be achieved.[15] This process is called thermalization. Once free electrons are in thermal equilibrium, at a temperature T_e, energy will be transferred to the lattice, which possess temperature $T_i < T_e$, through electron-phonon relaxation and thermal diffusion. During this process, energetic electrons collide with the lattice and since thermal energy is transferred to phonons, T_e decreases while T_i increases until they reach a common value. This leads to a modulated T_i profile which is locally beyond melting temperature, T_{melt}, and thus resulting in material transport, in means of phase transition of the material, and finally in resolidification of irradiated surface.[2], [7], [15]

Classification origin	Orientation	Period Λ	Representation in Fourier space	Type of LIPSS	Materials
Type-s SEW, SPP, radiative fields	⊥	$\approx\lambda$	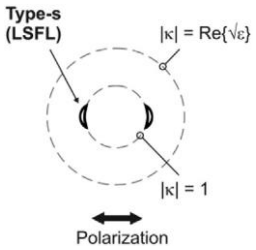	LSFL-I	metals, semiconductors
Type-d RR, "far-field" scattering, radiative fields	∥	$\approx\lambda/\mathrm{Re}(\sqrt{\epsilon})$	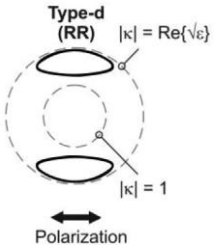	LSFL-II	semiconductors, dielectrics
Type-m RR	∥	$\approx\lambda$	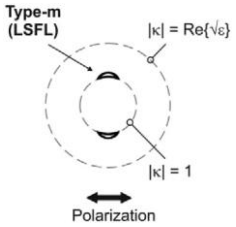	LSFL	
Type-r near-field scattering, nonradiative fields	⊥	$\approx\lambda/[2\mathrm{Re}(\sqrt{\epsilon})]$	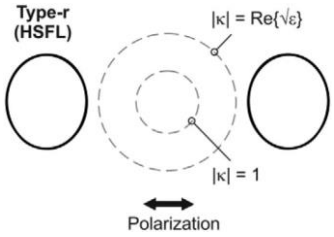	HSFL-I	semiconductors, dielectrics
Type-2s SEW, SPP with electric field redistribution	⊥	$\approx\lambda/2$	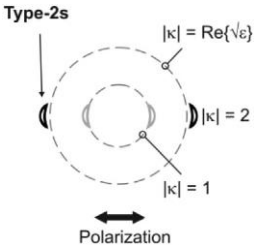	split LSFL-I	metals, semiconductors
Type-g scattering	∥	$> \lambda$	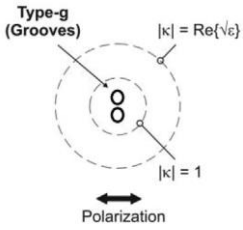	grooves	metals, semiconductors

Figure 9. Classification of different types of LIPSS summarizing their characteristics (orientation to polarization, spatial period Λ), their qualitative representation in Fourier space, and the materials involved. The two dashed circles in the Fourier space mark spatial frequencies $|\vec{\boldsymbol{\kappa}}| = \lambda/\Lambda = 1$ and $|\vec{\boldsymbol{\kappa}}| = \lambda/\Lambda = \mathrm{Re}(\sqrt{\boldsymbol{\varepsilon}})$. Image reproduced from Ref. [4]

Material transport is studied with the aid of hydrodynamic theories, that assume a molten state of the irradiated material.[4] In Fig. 10, a schematic of the aforementioned considerations is presented, while in Fig. 11 characteristic timescales of various electron and lattice processes in ultrafast laser-excited materials are depicted.

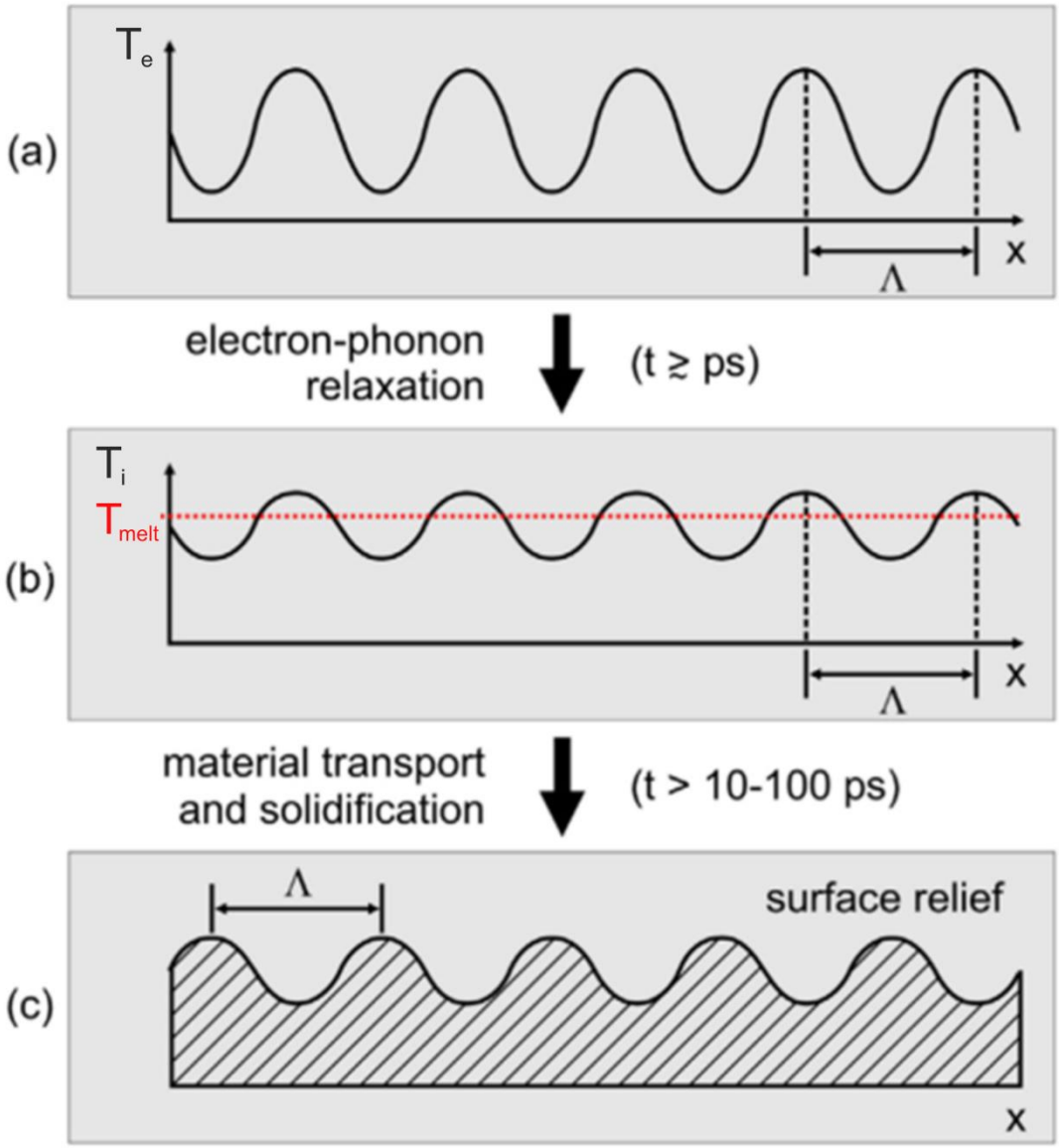

Figure 10. Scheme of LIPSS formation based on the TTM: a) The interference between the laser beam and the SEW electromagnetic field is assumed to induce spatially modulated electron density and electron temperature, T_e, profiles with the period Λ. b) The subsequent coupling of the electronic system and the lattice of the solid through electron-phonon coupling and thermal diffusion leads to a modulated lattice temperature, T_i, profile that locally exceeds melting temperature, T_{melt}. c) Selective ablation, material transport, and resolidification result in the final LIPSS pattern (surface relief). Image reproduced from Ref. [4]

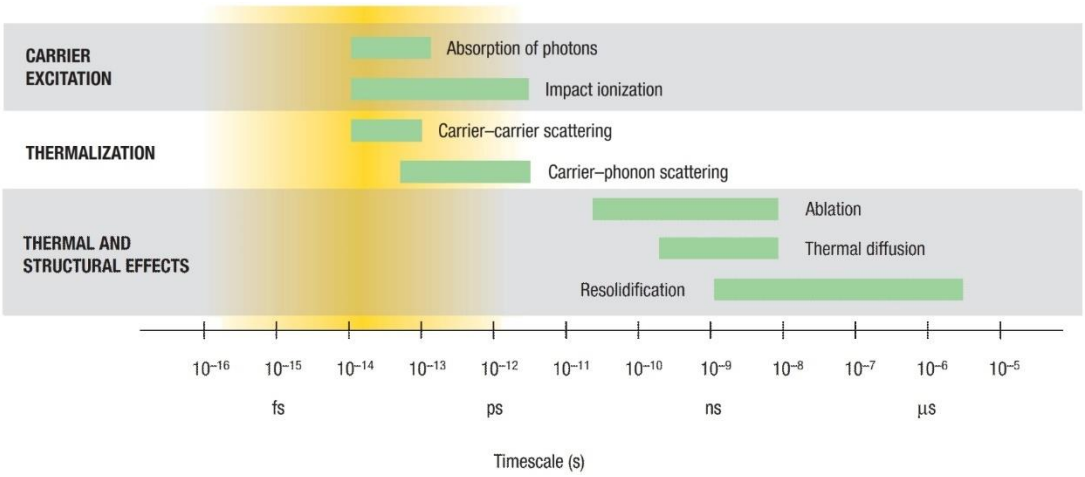

Figure 11. Timescales of various electron and lattice processes in laser-excited solids. Each green bar represents an approximate range of characteristic times over a range of carrier densities from 10^{17} to 10^{22} cm^{-3}, while yellow bar represents time duration of ultrashort pulse. Image reproduced from Ref. [7]

2.2.1. Surface Plasmon Polariton Waves (SPPs)

Since LIPSS periodicity and orientation always depend on the polarization direction of the incident electric field, it can be inferred that they originate from an electromagnetic mechanism leading to a spatially modulated deposition of the laser pulse energy. However, the period of LIPSS is predicted as a function of specific irradiation parameters and material properties. For the excitation of SPPs, on the one hand, an interface is required between a dielectric, most commonly air, and a metal, with dielectric permittivity ε_d and ε_m for bulk dielectric and bulk metal, respectively. On the other hand, when the laser sources employed are emitting at the near-infrared (NIR) regime of electromagnetic spectrum, as is the case in this thesis, SPPs are only excited when $Re(\varepsilon_m) < -1$. This requirement is commonly referred to as "SPP activity" and is fulfilled for all metals in NIR. However, under intense-irradiation conditions, initially plasmonically nonactive materials, semiconductors and dielectrics, can transiently be turned into a metallic state (plasmonically active). The reason why interference of SPPs with incident laser radiation is considered the most prominent mechanism for LIPSS formation, is due to its universal applicability in an extensive range of materials irradiated in NIR, when the aforementioned conditions are fulfilled.[4], [16]

SPPs are electron density waves, that result from coupling of incident light with surface plasmons, which are periodic waves that represent the spatial distribution of electric charge in the surface of a metal. They are confined in the vicinity of the interfaces and thus propagating only on borders along them, and

are damped out on both sides. In Fig. 12, the simple interference theory of coupling of SPPs with incident laser beam leading to LIPSS formation is presented. Through SPP model the predicted periodicity of LIPSS is described by:

$$\Lambda = \Lambda_{SPP} = \lambda \times \mathrm{Re}\left\{\sqrt{\frac{\varepsilon_m+\varepsilon_d}{\varepsilon_m\varepsilon_d}}\right\} \quad (3).$$

However, equation (3) is valid only for very small number of pulses, because at higher number of pulses there is a deviation, i.e., LIPSS periodicity drops at higher excitation levels and number of pulses.

Furthermore, due to the different dispersion relations of SPPs and incident photons, for a given laser frequency, a photon propagating in free-space has a smaller momentum than the SPP.[17] Thus, the requirement of initial microroughness on the surface of material aids for increased momentum of the incident photons in order to couple with surface plasmons. Also note that as is evident from equation (3), the periodicity of LIPSS originating from interference of SPPs with incident laser beam depends on the excited carrier density, N_e, since ε_m explicitly depends on free electrons density.[18], [19]

Although LSFL-I can sufficiently be explained with this SPP model of LIPSS, however it fails to account for HSFL with periodicity $\Lambda << \lambda$, since only near-wavelength periodicities are predicted with this approach, restricted by period of SPP waves.[4], [17], [20]

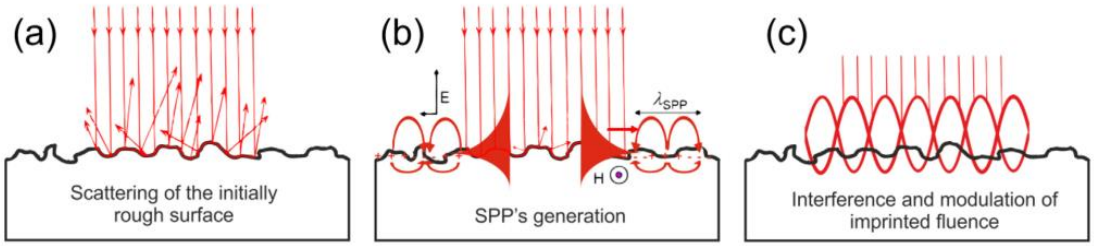

Figure 12. Scheme of electromagnetic formation mechanisms of LIPSS. The laser radiation (red) impacts the sample from the top. Its initial surface roughness results in (a) optical scattering that may lead to excitation of (b) SPPs that interfere with the incident light and modulate the absorbed fluence pattern "imprinted" in the material. (c) Finally, modulated ablation results in periodic surface structures. Image reproduced from Ref.[4]

2.2.2. Second Harmonic Generation (SHG)

One of the most common proposed mechanisms for the formation of HSFL is due to second harmonic generation (SHG). SHG, also called frequency doubling, is highly likely to occur under extreme irradiating conditions and is a nonlinear process, in which two photons, of the same frequency, interacting with a nonlinear material are effectively "combined" to form a new photon that has twice the frequency of initial photons. Since the frequency of final photon has doubled, its wavelength has been reduced to half with respect to the wavelength of initial photons. By taking into consideration these alterations in the properties of materials, induced due to high intensities of electromagnetic fields, the response of dipole per unit volume in an applied electric field will change, thus leading to significant excitation of near-field scattered waves, that couple with incident irradiation.[21]

3. Experimental Methods and Materials

Although surface modification with laser nanostructuring is a simple, efficient and fast technique, several considerations of laser-matter interaction must be taken into account. In order to induce grating-like periodic nanostructures of desired orientation and periodicity on surfaces, irradiating source's parameters such as wavelength, pulse duration, pulse energy, focal spot size, polarization state, number of pulses and repetition rate are of great importance and when not appropriate, they are able to significantly affect the features of modified topography.[9], [20], [22] Since this is the case, these parameters must be handled carefully and, moreover, they should be optimized according to the solid material and irradiation conditions. However, the aim of this thesis is to analyze how periodicities of HSFL, once these periodic nanostructures are formed, are evolving, only when pulse energy and number of pulses are varying. Hence, in this section, the laser beam parameters, instrumentation, dynamic surface processing and characterization methods are discussed in detail.

3.1. Laser beam spatial profile – Gaussian beams

In optics, Gaussian beams are beams of electromagnetic radiation whose amplitude envelope in the traverse plane implies a Gaussian intensity profile. A major feature of Gaussian beams is their high monochromaticity and they can be roughly assumed as an intermediate wave between plane and spherical waves. Since both of these kinds of electromagnetic waves are not actually feasible, Gaussian beams are employed instead, in many applications. Especially, the fundamental transverse Gaussian mode, also called TEM_{00}, describes in most cases the desired output of commercial lasers, since it can be focused into the most concentrated spot. Assuming that such an electromagnetic wave propagates along +z-axis and its polarization is in x direction, the distribution of electric field is described by:[23]

$$\vec{\mathrm{E}}(\vec{\mathrm{r}}) = \mathrm{E}_0\, \hat{\mathrm{x}}\, \frac{\mathrm{w}_0}{\mathrm{w(z)}}\, \mathrm{e}^{\left(\frac{-\mathrm{r}^2}{\mathrm{w(z)}^2}\right)}\, e^{\left[-i\left(kz + k\frac{r^2}{2\,R(z)} - \psi(z)\right)\right]} \tag{4}$$

where

- r is the radial distance from the center axis of the beam,
- z is the axial distance from the beam's focus (or "waist"),
- i is the imaginary unit,

- $\vec{k} = \hat{z}\, 2\pi n/\lambda$ is the wave number for a free-space wavelength λ, and n is the refractive index of the medium in which the beam propagates,
- $E_0 = E(0,0)$ is the electric field amplitude (and phase) at (r = 0, z = 0),
- w(z) is the radius at which the field amplitudes fall to 1/e of their axial values, and intensity values fall to $1/e^2$, respectively, at the plane z along the beam. It is also called the waist at z,
- $w_0 = w(0)$ is the waist radius at z = 0,
- R(z) is the radius of curvature of the beam's wavefronts at z, and
- ψ(z) is the Gouy phase at z, an extra phase term attributable to the phase velocity of light.

However, as indicated from equation (4), the profile of electric field distribution does not stay constant as the beam propagates through space, hence the

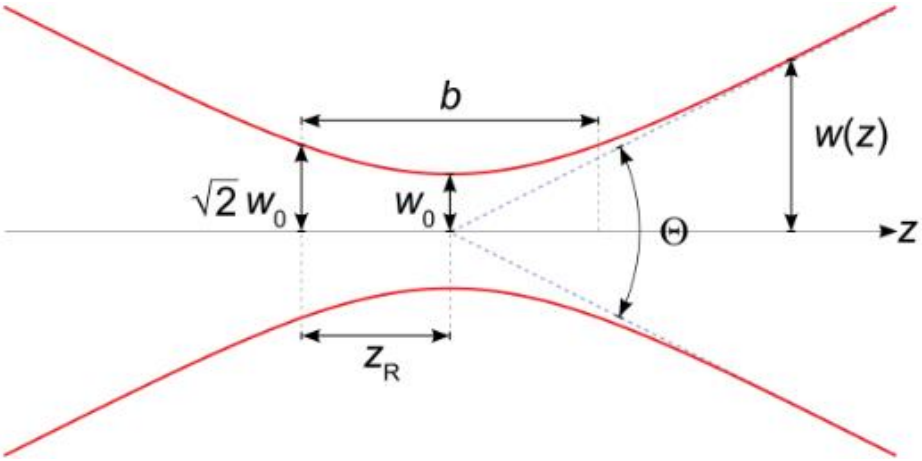

Figure 13. Schematic of a focusing Gaussian beam propagating along z-axis. Image reprinted from Wikipedia commons.

dependence of w(z) on z. Due to diffraction, a Gaussian beam will converge and diverge from the beam waist, w_0, which is where the beam diameter reaches a minimum value. In Fig. 13, a schematic of a focusing Gaussian beam which propagates along +z direction is presented and the most important quantities mentioned above are depicted.

Due to its importance on calculations, the beam waist at z = 0, w_0, can be theoretically predicted. The theoretical beam radius of a collimated laser beam after passing through a converging lens is expressed by the following equation:

$$w_0 = \frac{2\, f\, \lambda\, M^2}{\pi\, D} \tag{5}$$

where

- f is the focal length of the focusing lens
- λ is the wavelength of the laser
- M^2 is the beam quality factor, which compares the performance of a real laser beam with that of a diffraction-limited Gaussian beam, and
- D is the diameter of the collimated input laser beam onto the converging lens.

Furthermore, as is evident from Fig. 13, Gaussian irradiance profiles are symmetric around the center of the beam and decrease as the distance from the center of the beam perpendicular to the direction of propagation increases. The latter consideration is seen in Fig. 14.

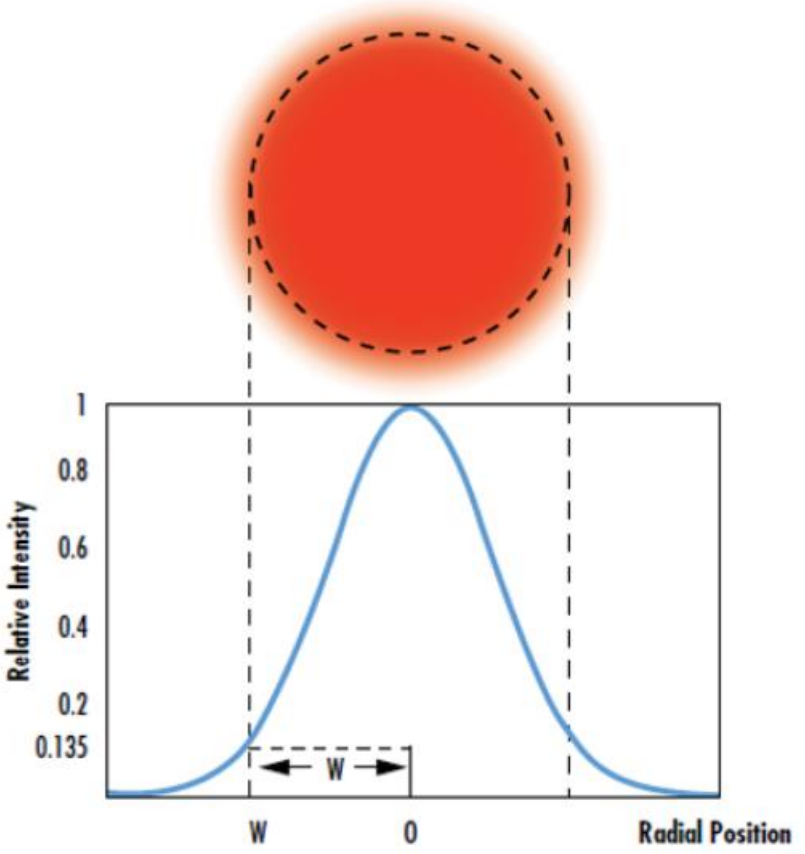

Figure 14. The waist of a Gaussian beam is defined as the location where the irradiance is $1/e^2$ of its maximum value. The dashed circle indicates the borders of this location. Image reprinted from (https://www.edmundoptics.eu/knowledge-center/application-notes/lasers/gaussian-beam-propagation/)

For a Gaussian beam, the spatial profile of pulse fluence along the diameter of the beam, is $F \propto \left|\vec{E}\right|^2$ and is given by:

$$F(\vec{r}) = \frac{2\,E_p}{\pi\, w(z)^2}\, e^{\left(-\frac{2\,r^2}{w(z)^2}\right)} \tag{6}$$

where E_p is the pulse energy. The maximum fluence occurring within the Gaussian profile is when r = 0 and is commonly named as peak fluence. Considering that z = 0, laser peak fluence is calculated from:

$$F_0 = \frac{2\,E_p}{\pi\, w_0^2} \tag{7}$$

In order to experimentally measure the beam waist or spot size, w_0, Liu et. al in 1982 proposed a simple method, by which the beam waist is estimated from the slope arising from a fitting procedure.[24] More specifically, according to their approach the spot size of the Gaussian beam can be calculated from the fabricated craters produced by ablation after irradiation of a sample. Considering the actual laser damaged craters radius profiles r_a and r_b, vertical and horizontal radius, respectively, and plotting the following relations:

$$E_a = E_p\, e^{\left(-\frac{2\,r_a^2}{w_0^2}\right)}$$

and

$$E_b = E_p\, e^{\left(-\frac{2\,r_b^2}{w_0^2}\right)} \tag{8}$$

an extracted dependence of r_a to r_b can be expressed as:

$$r_a^2 = \frac{w_0^2}{2} \ln \frac{E_p}{E_a}$$

and

$$r_b^2 = \frac{w_0^2}{2} \ln \frac{E_p}{E_b} \quad (9)$$

The beam spot size can then be extracted by plotting average r^2 versus $\ln \frac{E_p}{E_{avg}}$, where E_{avg} is the average pulse energy, and by estimating the slope of the plot, through linear fitting. Then the slope is equal to $\frac{w_0^2}{2}$, which can be solved for w_0. Although in this thesis this quantity is derived in a somewhat different manner, this method of Liu is extensively used in literature for the spot size measurement, and was worth mentioning for the sake of completeness.

3.2. Dynamic surface processing with Gaussian beams

Dynamic surface processing is defined as repetitive irradiations in a single or multiple directions with laser pulses. In this case, the sample is assumed to be in constant motion with controlled velocity on the x and y axes, while the position on z-axis is fixed. LIPSS are also, usually, a multi-pulse phenomenon, where inter-pulse feedback plays an important role. Under static irradiation, that is that the sample does not move on either x or y direction, for the irradiation of a single spot at the surface by N consecutive laser pulses, each location is hit N times with the identical fluence value. As a consequence, distinct, spatially separated surface regions covered by different types of LIPSS can be observed. For the case of line scanning with focused laser pulses, the concept of the effective number of pulses per spot, N_{eff}, must be introduced in order to account for spatial overlapping of consecutive laser pulses as the sample moves. Upon scan-processing of 1D lines, that are typically performed at a constant scan velocity, due to a nonzero pulse-to-pulse spot overlap, a fixed location at the surface is exposed to different local laser fluences as the sample moves. As irradiation starts, a surface location in the vicinity is firstly exposed to reduced local laser fluence from the rising tail of the Gaussian laser beam profile. As the sample is slightly displaced, increased fluence values from the most intense part of the Gaussian profile will radiate the location and with further displacement, finally, the falling edge of the laser beam profile will hit the specific location. The total amount of fluence that irradiates this arbitrary location within the 1D line is defined except from laser fluence, by the laser repletion rate and scanning velocity and therefore from pulse-to-pulse

overlapping. 2D areas can, as well, be processed by meandering displacement of 1D lines in the orthogonal direction. In this case, except from pule-to-pulse overlapping along x direction, the selection of hatch on y direction is of crucial importance, and hence, additional exposures manifest at the selected surface location through the scanning of multiple overlapping lines. In such a scanning approach, surface structures formed in the high fluence part of the scanned beam can later be "overwritten" by the low fluence tails of the Gaussian beam profile, often resulting in micro- to nano-structures with different types of LIPSS being superimposed.[4]

To allow for a roughly comparison of spot, line and area processing with a pulsed laser beam, the equations defining N_{eff} are presented below:

$$N_{eff,1D} = \frac{2\,w_0}{\Delta x} = \frac{2\,w_0\,f}{v_x}$$

and

$$N_{eff,2D} = \frac{\pi\,w_0^2\,f}{v_x\,\Delta y} \tag{10}$$

for 1D and 2D scanning processing, respectively.

In equations (10):

- f is the laser repetition rate
- Δx is the displacement in x direction, and if $0 < \Delta x < 2w_0$ then the pulse-to-pulse overlap is nonzero
- v_x is the constant scan velocity in x direction, and
- Δy is the hatch in y direction. If $0 < \Delta y < 2w_0$ then the line overlapping is nonzero.

In Fig. 15, a schematic representation of the concept of effective number of pulses per spot is illustrated for the case of 2D area scanning processing, while 1D line processing and static processing can be conceived by analogous simplifications in this scheme.

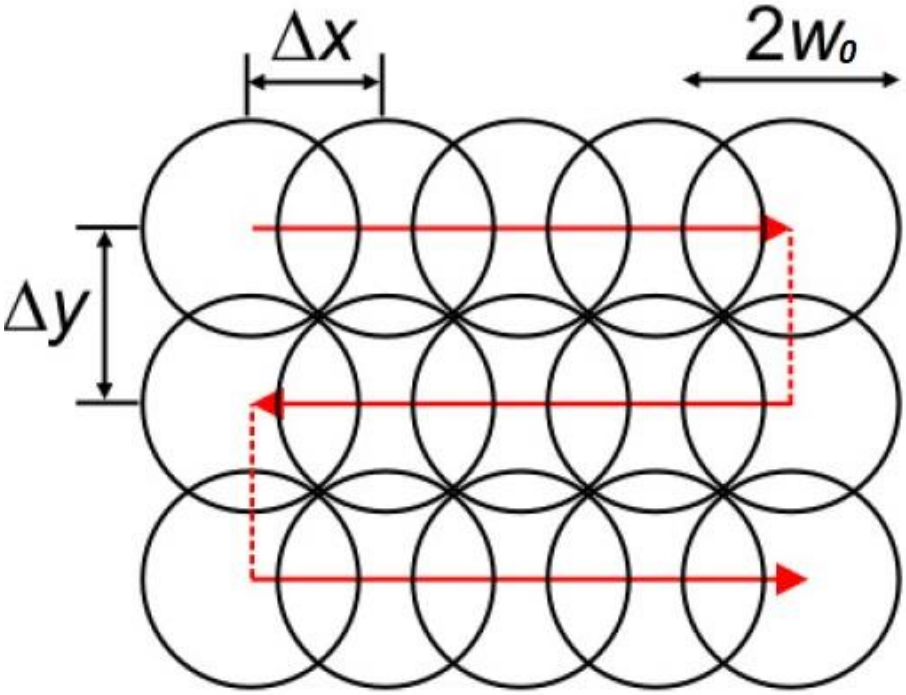

Figure 15. Schematic representation of 2D area scanning processing, with nonzero pulse-to-pulse overlapping and line-overlapping. The red arrows indicate the scanning path. Image reproduced from Ref. [37]

3.3. Experimental apparatus

The experimental layout consists of three parts: the laser source, the optical path along with the processing apparatus and the parameter-measuring setup. Particularly for the first two, the general experimental setup developed and utilized for the laser nanostructuring of all samples in this thesis is schematically presented in Fig. 16. Both a Pharos-SP laser source from Light Conversion with Yb:KGW as active medium was used to produce linearly polarized pulses of pulse duration 170 fs (ultrafast source) with tunable repetition rate ranging from single shot to 200 kHz and 1026 nm central wavelength (NIR) and an OneFive Origami XPS laser source from NKT Photonics was employed to provide linearly polarized pulses of pulse duration 350 fs (also ultrafast source) with tunable repetition rate varying from single shot to 800 kHz and central wavelength 1030 nm (NIR). For both laser sources, the rest experimental treatment of the laser beam within the optical path is identical. Upon its emission, the laser beam is aligned through systems of mirrors with irises (not shown in Fig. 15), that are placed in many different places of the optical path, in order to achieve alignment of high accuracy. These systems of mirrors elevate and direct the beam into the processing setup, where the optics are mounted in such a way that the beam hits perpendicularly the samples. Moreover, the final part of the processing setup consists of a zero-order half-waveplate in series with a polarizing beam splitter cube in order to serve as an attenuator and in order to

provide p-polarized light (linear polarization in the x direction). At last, the laser pulses are focused on the surface of each studied sample via a plano-convex

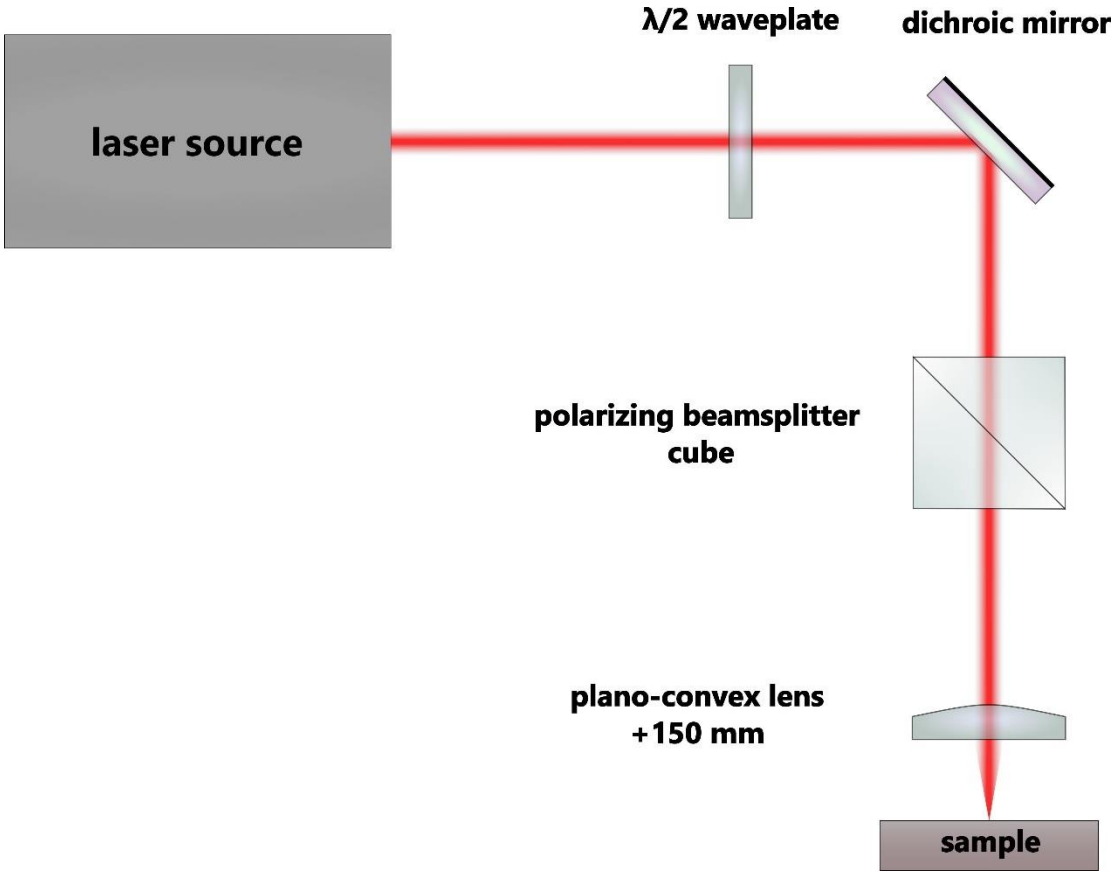

Figure 16. Schematic representation of the experimental setup developed and utilized to conduct all of the experimental procedures.

lens of 150 mm length. The samples are mounted on top of a xyz motorized servo stage from Newport, that allows translation on both x, y and z direction.

The movement of the stage and laser irradiation are controlled through a LabVIEW program.

The parameter-measuring setup refers to all the media used for measuring the output parameters, such as beam waist on focus of lens (spot size) and laser power. The spot size is determined with the aid of a CMOS camera, which is absorbing for NIR, within the Rayleigh length of the focal plane at $1/e^2$, and is measured ~ 45 μm for the Pharos-SP laser source and ~ 59 μm for the Origami XPS laser source, respectively. Furthermore, the average power is measured with a Ge-based photodiode power sensor, that is adjusted to the optical path in the vicinity of focal plane of the plano-convex lens, when needed.

3.4. Material targets

3.4.1. Cleaning protocols

For the purposes of this thesis, the samples used as targets are all bulk. Parametric studies were conducted on single crystal, (1 0 0), one-side-polished, boron-doped p-type silicon wafers with a thickness of 525 μm, one-side-polished nickel substrate of 300 μm thickness and a molybdenum substrate with a thickness of 500 μm, which was mechanically polished on both sides.

Before irradiation, all bulk materials were cleaned with ethanol dilution of purity >= 99.8% for 10 minutes in ultrasonic bath and were dried with gaseous nitrogen. After irradiation, silicon wafers were sunk into hydrofluoric acid (HF) dilution of 20% purity for 15 minutes, so that, due to etching, recast matter and nanoparticles, especially oxides, at the borders and within the structures would be removed. Finally, all substrates were cleaned with high purity, >= 99.8%, acetone dilution for 15 minutes in ultrasonic bath and were dried with gaseous nitrogen. This way, every material residual that was ejected due to laser ablation was extracted, leaving the surface of the material completely clean.

3.4.2. Conditions of irradiation

After being mounted on the stage normal to incident radiation, the priority was to search for the focus of lens with respect to the material subjected to irradiation. This step was of great importance, because each sample had different thickness and absorptivity. So, to seek for the position on z-axis, where each material absorbed most efficiently the pulse energy, samples were irradiated under arbitrary, but above the ablation threshold, pulse energies to induce discrete and displaced craters on the surface, while the stage was elevating after each perspective irradiation. At last, after having obtained this optimal position in z-axis for each sample, the stage was translated there, and was kept constant throughout each irradiation of the respective material. It has to be noted, that irradiations throughout all experiments were conducted under ambient conditions, that is in air.

Afterwards, a parametric study on each sample was conducted with 1D line scanning processing. Lines of 500 μm, 300 μm and 1000 μm width each, were patterned on the surface of silicon, nickel and molybdenum, respectively. Every line was irradiated under different laser conditions, so to allow for the investigation of the behavior of ripples' periodicity as either fluence or effective number of pulses per spot changes. In Table 1, the materials used as targets and some irradiation parameters are summarized.

Material	Thickness	Irradiating laser source	Irradiation parameters
Bulk Silicon (Si)	525 μm	Pharos-SP	200 kHz, 1026 nm, 170 fs
Bulk Nickel (Ni)	300 μm	Pharos-SP	1 kHz, 1026 nm, 170 fs
Bulk Molybdenum (Mo)	500 μm	OneFive Origami XPS	10 kHz, 1030 nm, 350 fs

Table 1. Summarized materials used as targets for irradiation and surface modification with ultrashort laser pulses.

3.5. Characterization methods

The laser fabricated structures on the surface of irradiated samples and surface modifications were depicted through the aid of optical microscopy, scanning electron microscopy (SEM) and atomic force microscopy (AFM).

An optical microscope was utilized in order to roughly decide for the focus of lens on irradiated material. The position of stage, where the irradiated sample absorbed the pulse energy more efficiently, was determined through optical microscopy by observing the characteristics of discrete patterned craters. These craters were induced on the surface of solid materials by changing the distance between the lens and stage, and hence, the most appropriate distance for optimized absorptivity was attributed to the most homogeneous, circular and smallest spot.

However, due to diffraction-limited resolution of optical microscopes, only near-wavelength LSFL structures could be observed. HSFL ripples, which are the focus of this thesis, with periods smaller than wavelength and thus, well below the diffraction-limit, could not be obtained. Therefore, a high-resolution scanning electron microscope (JEOL JSM – 7000F), that reached even down to the nanometer scale, was employed. Nevertheless, each sample that was to be examined with SEM, had to be completely clean and this is the reason of aforementioned thorough cleaning after irradiation. Furthermore, SEM operates under high-vacuum conditions, and its best performance is assured when a sample is perfectly clean. Another consideration for high-resolution SEM images is that the sample has to be conductive. An insulating material would accumulate electron charge on its surface due to incident electron beam, and if this is the case the image would get blurry. To overcome this limitation, insulating samples have to undergo sputtering, a technique by which a thin layer of conductive material, commonly Au, is deposited on the modified surface. Hopefully, in this study only conducting solid materials were studied,

so there was no need for special treatment of the samples. After all, SEM provided images with 1280 × 1024 resolution that were analyzed for the periodicity of HSFL structures with methods that will be discussed in detail in the following subsection. The magnification of each retrieved image was such that the nanoripples and modified topography were obvious and distinguishable

Finally, AFM was employed in order to confirm HSFL periodicities and to measure the height of these ripples, so to classify them among HSFL-I or HSFL-II. A high-resolution atomic force microscope (BRUKER-ICON), able to track protrusions of the order of ~ Å was employed, in order to depict the topography of surfaces. The limitations of this instrumentation, is that it cannot detect height differences of ~ 10 μm and the sample to be scanned needs to be flat. AFM involves a scanning probe with a sharp tip, that follows a raster path while tracking the surface. The sharp tip is integrated near the free end of a flexible cantilever and as the tip moves over features of different height the deflection of the cantilever changes. Finally, the coordinates that the tip tracks during the scan are combined to generate a three-dimensional topographic image of the surface. Surfaces of (3 x 3) μm^2, (1.5 x 1.5) μm^2 and (3 x 3) μm^2 on silicon, nickel and molybdenum, respectively, were scanned.

3.5.1. Periodicity measurements

As previously implied, SEM and AFM were employed in order to estimate HSFL periodicities and features sizes (height, depth, etc.), respectively. For this purpose, the SEM and AFM images of the modified surfaces were examined through image analysis opensource programs, such as ImageJ and Gwyddion. The exact procedure of the subsequent analysis is presented in the following paragraphs.

In order to be able to retrieve spatial frequency information, a 2D fast Fourier Transform (2D-FFT) was employed. Each SEM image can be analyzed through its transformation into a two-dimensional fast Fourier transform map. Hence, Gwyddion was used, which is a program that transforms the imported SEM image to a reverse space image via a 2D-FFT algorithm. The map that is generated is the spatial display of the intensity of the frequency in the reverse space. In Fig. 17a, a typical SEM image of an irradiated line with horizontal electric field polarization is presented along with its corresponding Fourier-transformed space image, in Fig. 17b. In Fig. 17b the green line indicates the direction vertical to the ripple nanostructure.

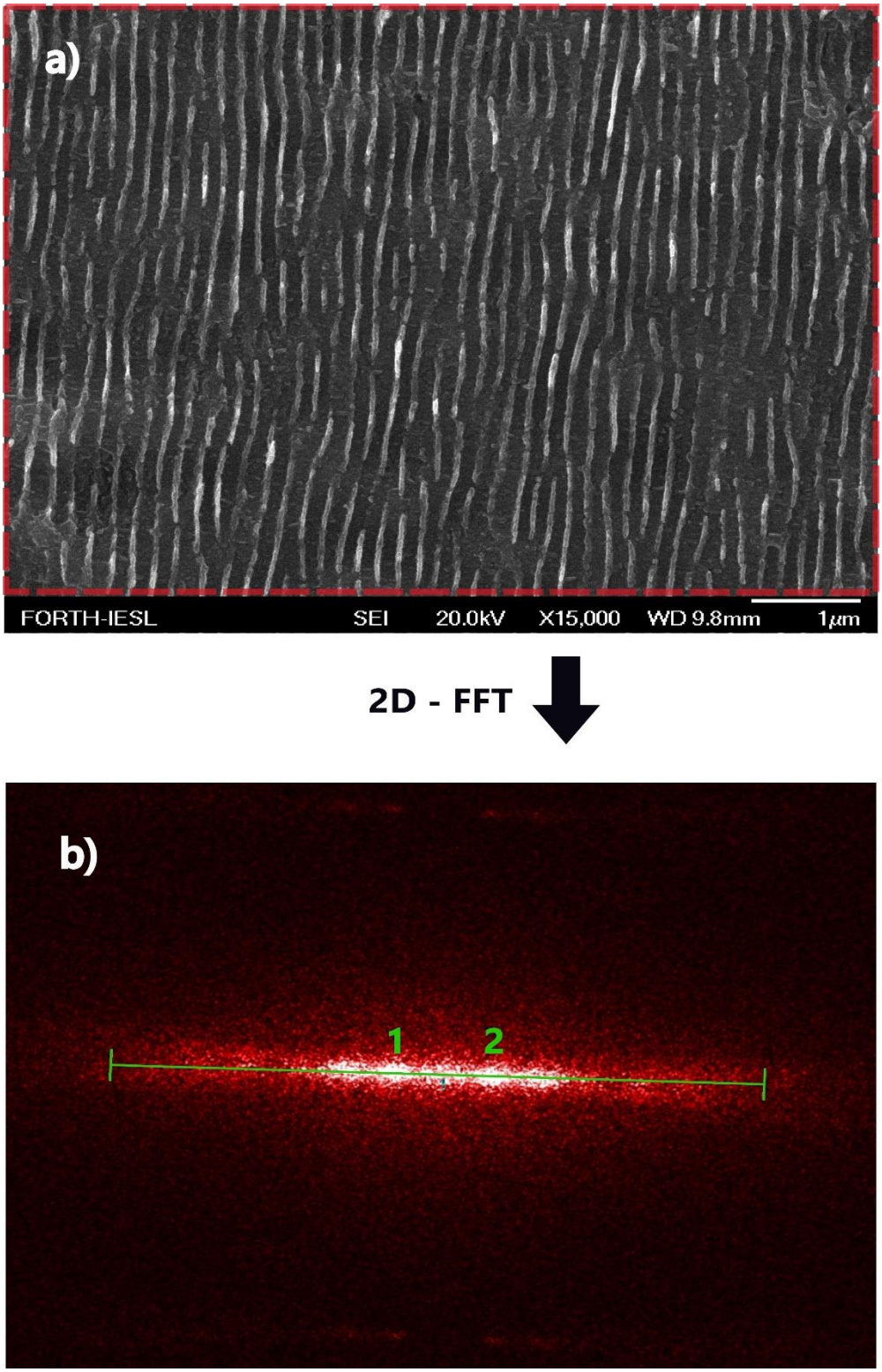

Figure 17. a) SEM image of HSFL formation on silicon surface, b) corresponding 2D – FFT of the area inside the red-dashed box. The 1 and 2 green labels indicate the attained characteristic frequencies on Fourier space.

Along this direction, the Fourier transformation "detects" a periodical fluctuation of the frequency intensity. This fluctuation exhibits an average frequency which is inversely proportional to the average HSFL period. In order to calculate the periodicity of HSFL, Λ_{HSFL}, the profile of these frequencies along this vertical to HSFL direction should be plotted. The occurring diagram consists of vertical peaks that can be fitted through the Lorentzian distribution. The fitting of Lorentz function then produces the position of maximum value and the linewidth for each Lorentzian fit curve. The profile along the green line in Fig. 17b corresponds to the intensity-frequency diagram depicted in Fig. 18. In this figure, the Lorentz fit in the 1st peak is illustrated.

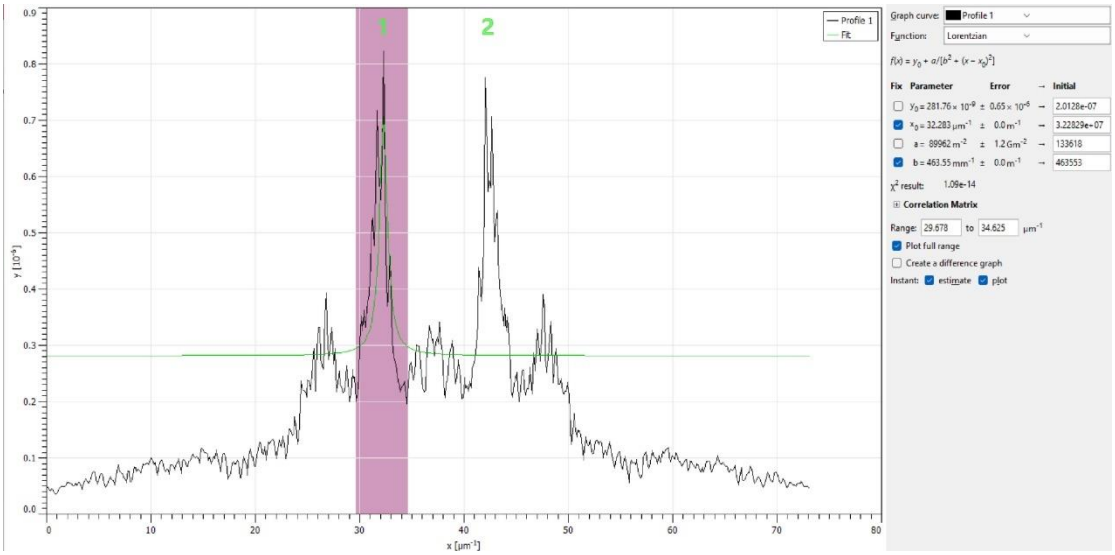

Figure 18. Lorentz fit of the peak intensity of frequency along the cross-section of Fig. 16 b). 1 and 2 green labels are reproduced here for the sake of convenience.

Generally, the profile of the FFT image along a specific direction may consist of many peaks. However, when accounting for periodical surface modification, there will always be intensity frequency peaks (1 and 2 in Fig. 17b and 18) equally spaced on both sides of a central one. This means that the corresponding frequency is also the most prominent one. In order to calculate the average periodicity of the structures, Λ, the positions of the frequency peaks should be firstly derived, through Lorentzian fitting as described above.

Assuming that f_1 corresponds to the position of the 1st peak and f_2 of the 2nd, respectively, then average periodicity is deduced from:

$$\Lambda = \frac{2}{|f_2 - f_1|} \tag{11}$$

while

$$\delta\Lambda = \frac{(b_1 + b_2)}{2\,|f_2 - f_1|^2} \tag{12}$$

where b_1, b_2 are the linewidths for the two Lorentzian fit curves of the 2D-FFT image profile peaks.

With this method for derivation of average periodicity, i.e. through SEM images and corresponding 2D-FFT transformation, well established, structures' periodicities were verified also via AFM images. To estimate the spacing of ripples with this approach, ImageJ was employed in order to measure the appropriate peak-to-peak distances (along the horizontal axis). However, as distances are initially measured in pixels, a scalebar indicating a known distance in μm is provided to accurately convert pixels into μm. An AFM image, for the same irradiating conditions as in Fig. 17, is provided in Fig. 19.

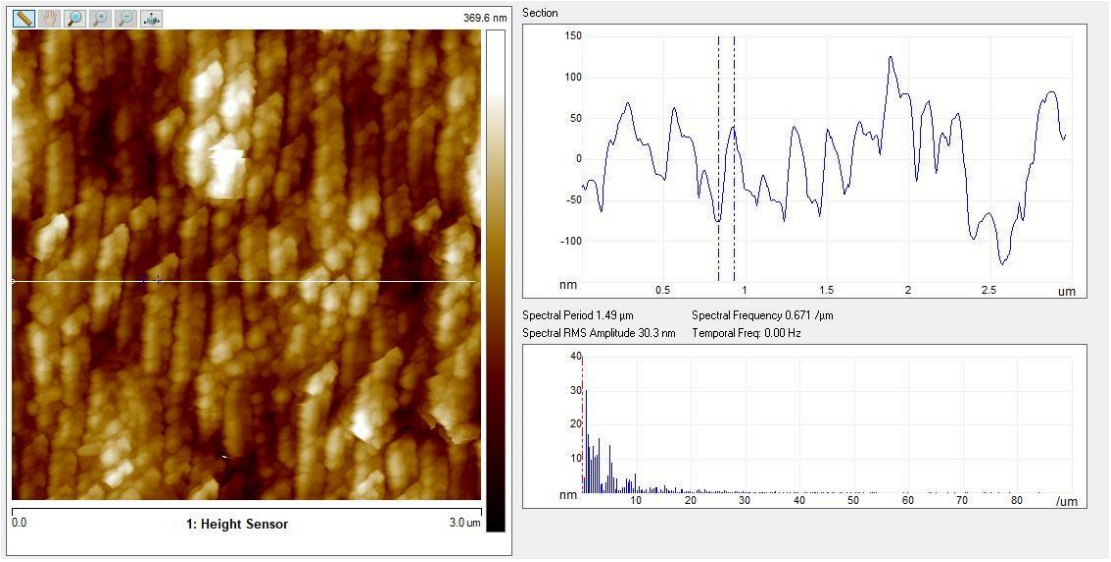

Figure 19. AFM image retrieved from silicon surface irradiated under the same conditions as in Fig. 17. The left image indicates the scanned-surface's topography and the cross-section height profile is illustrated on the top-right image.

Finally, the average periodicity is estimated by averaging over the measured peak-to-peak distances and the corresponding uncertainty in measurements is evaluated through standard deviation.

3.5.2. Height measurements

AFM was also employed for height measurements, in a similar manner to period measurements. For this purpose, though, the height of each fabricated structure was measured, i.e. distances in vertical axis. Note that the scalebar in y-axis might be different, as was the case here. The average value for the height of ripples was estimated, again, by averaging over the measured heights and the error was set as the standard deviation.

4. Results and Discussion

A series of parametric studies have ben performed in order to attain the trend of HSFL periodicity on silicon, nickel and molybdenum surfaces under various laser conditions. A semiconductor and two metals were chosen to be studied in order to determine if there are differences on the induced surface topography with respect to, first of all, the class of irradiated material. Furthermore, the two metals were also studied, as nickel and molybdenum have different electron-phonon coupling factors (data were accumulated by: https://compmat.org/electron-phonon-coupling/). Specifically, as for molybdenum the electron-phonon coupling factor is ~ 15 times greater than the electron-phonon coupling factor of nickel, more uniform LIPSS were expected to be fabricated on the surface of molybdenum.

As it was expected, variation of the laser parameters, led to a variety of different morphologies at the micro/nanoscale. The laser parameters varying throughout the conduction of experiments were peak laser fluence, F_0, and effective number of pulses per spot, N_{eff}, under 1D scanning irradiation. In this section, the results for periodicity of HSFL, Λ_{HSFL}, covering the surface of a bulk semiconductor and bulk metals along with the evolution of this periodicity as F_0 and N_{eff} independently increase, will be presented and discussed in detail. Furthermore, accounting for the behavior of Λ_{HSFL} as F_0 and N_{eff} change, possible mechanisms will be proposed for the formation of HSFL on different substrates. Finally, as HSFL can be sub-classified into HSFL-I and HSFL-II with respect to their depth-to-period aspect ratio, the fabricated ripples on each sample will be characterized via AFM analyzed results and a 3D image of the modified surface will be provided.

4.1. Silicon

Silicon was chosen to be irradiated, as silicon surface processing with ultrashort pulsed lasers has received considerable attention over the past decade due to its important technological applications, particularly in industry and medicine.[25]–[27] In the work of Bonse et. al[20], some characteristic laser parameters are provided under which HSFL formation on silicon surface is achievable. Based on this report, the parametric study was conducted for N_{eff} ranging from N_{eff} =1000 pps (8.950 mm/s) to N_{eff} = 200000 pps (0.045 mm/s) and for F_0 ranging from F_0 = 0.16 J/cm^2 to F_0 = 0.80 J/cm^2; for somewhat extended ranges of both N_{eff} and F_0, in order to observe the transitions of induced morphologies on the surface topography. Fig. 20 illustrates a map of the patterns fabricated on silicon and some characteristic corresponding SEM images for each value of both N_{eff} and F_0.

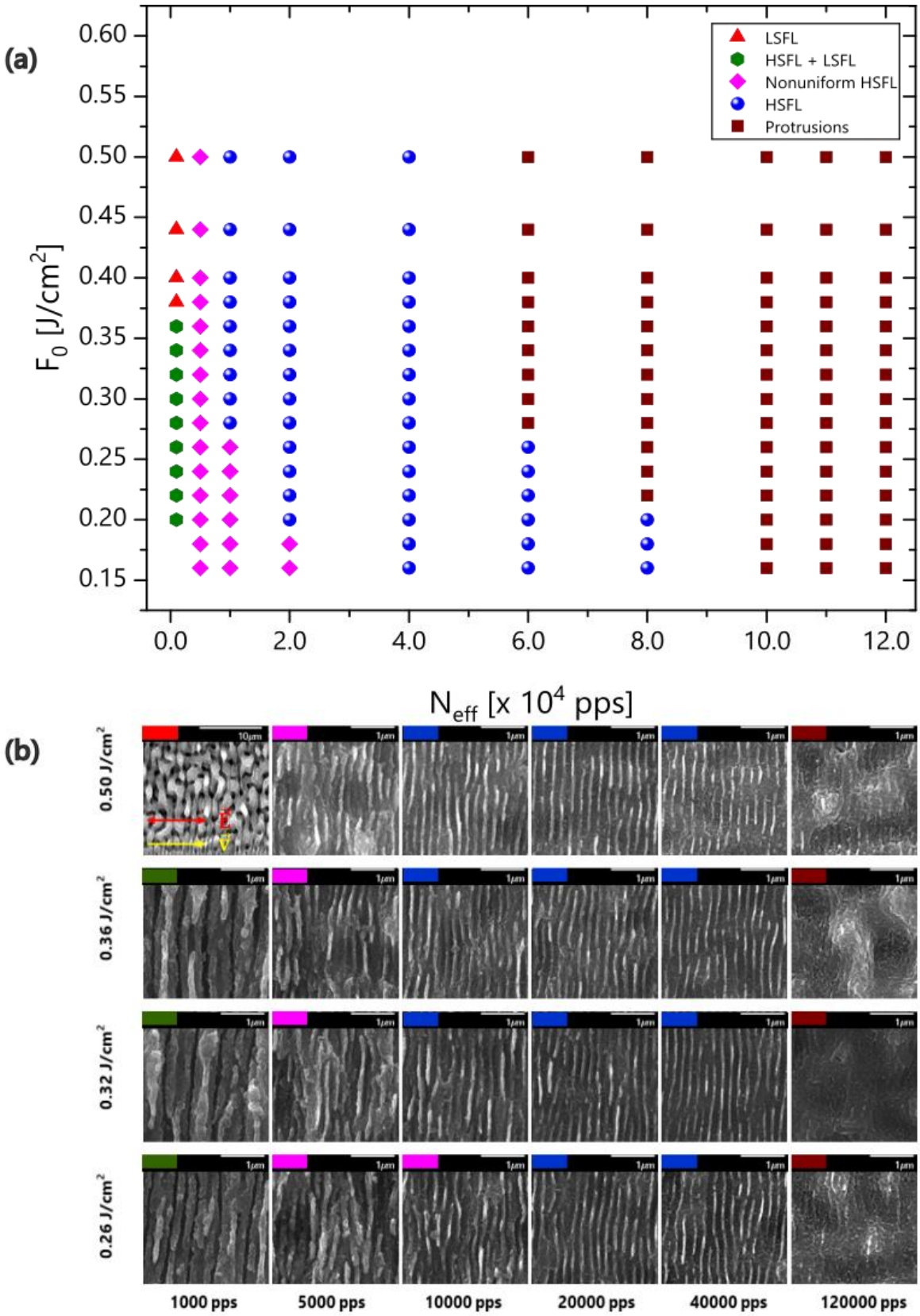

Figure 20. Map of the morphologies fabricated on silicon by linearly polarized beam scanning the irradiated surface with λ = 1026 nm, 200 kHz and Δτ = 170 fs. (a) Morphological map of silicon surface as a function of N_{eff} and F_0. (b) SEM images of the corresponding morphologies. Red double-ended and yellow arrows in (b) indicate the direction of laser polarization and of scanning velocity, respectively. The color of boxes on the top-left side of each image in (b) corresponds to coloration of structures in (a).

As is depicted, a variety of morphologies -LSFL, HSFL + LSFL, nonuniform HSFL, HSFL and protrusions- is patterned on silicon under these irradiating conditions. More specifically, for N_{eff} = 1000 pps both LSFL, with Λ_{LSFL} = (545 ± 27) nm, and LSFL in combination with HSFL are formed. This transient change on the morphology of modified surface is observed, for a specific value of N_{eff} as F_0 decreases. For the case defined as (HSFL + LSFL), the HSFL patterned on the surface of silicon seem to originate from the splitting of LSFL, with $\Lambda_{LSFL} \sim \lambda/2$, thus a periodicity of $\Lambda_{HSFL} \sim \lambda/4$ could be expected. The interpretation of the physical process that accounts for that will be explained in the next sections. As N_{eff} increases to 5000 pps (1.790 mm/s), nonuniform HSFL are fabricated, while uniform HSFL, termed, simply, as HSFL, are formed for N_{eff} ranging from 10000 pps (0.895 mm/s) to 80000 pps (0.112 mm/s) and in a peak fluence range of F_0 = 0.16 J/cm^2 to F_0 = 0.80 J/cm^2. As N_{eff} increases further up to 200000 pps the surface of silicon is covered with protrusions. The orientation of HSFL is found to be perpendicular to laser polarization, regardless of F_0 and N_{eff} and scanning direction, and is parallel to LSFL, that were formed with a smaller number of effective pulses per spot. In order to estimate the periodicity of HSFL via SEM images with the 2D-FFT method, the entire patterned area of SEM images was taken into account since HSFL covered it uniformly. Furthermore, data analysis of AFM images for the periodicity of HSFL indicated good agreement with the periodicities predicted via SEM images. Finally, the height of HSFL was, also, estimated by measurements conducted on the AFM images.

4.1.1. Periodicity of HSFL as a function of laser peak fluence

Well pronounced and homogeneous HSFL have been obtained by varying laser peak fluence in a range of F_0 = 0.16 J/cm^2 to F_0 = 0.80 J/cm^2, as illustrated in Fig. 20a. For silicon, this range of peak fluence includes irradiations under sub-melting fluence threshold (0.15-0.20 J/cm^2) for a single pulse[28], but also includes fluences exceeding the ablation fluence threshold (0.20-0.30 J/cm^2) for multi-pulses[29]. As is depicted in Fig. 21, Λ_{HSFL} tends to remain constant as a function of peak laser fluence for each different value of effective number of pulses per spot. However, this constant value decreases from Λ_{HSFL} = (229 $\pm$ 16) nm to Λ_{HSFL} = (179 $\pm$ 6) nm, as N_{eff} increase from N_{eff} = 5000 pps to N_{eff} = 80000 pps.

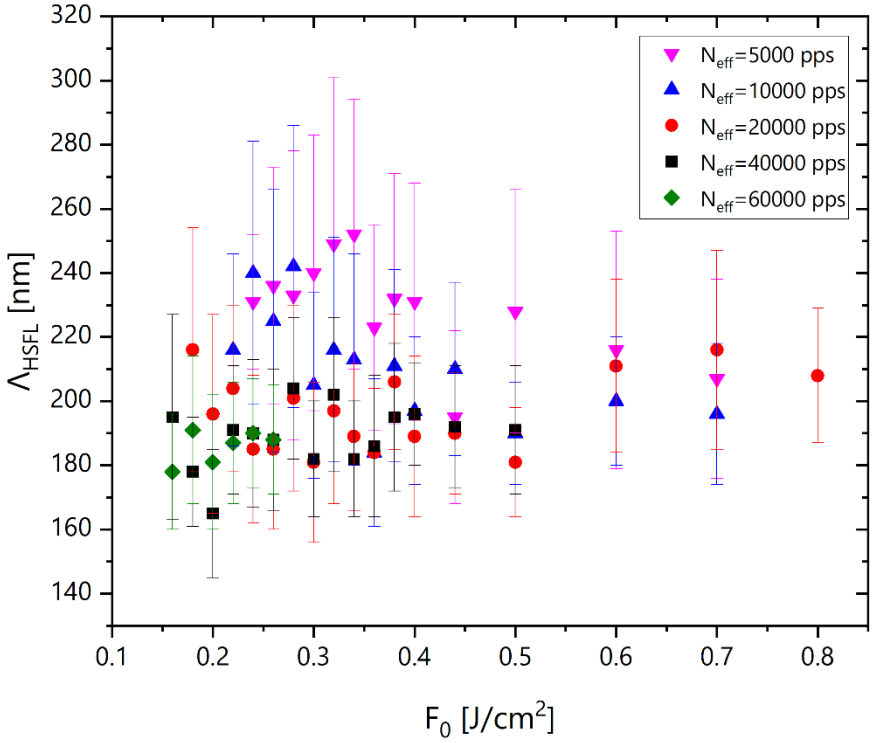

Figure 21. Periodicity of HSFL on silicon as a function of laser peak fluence, F_0. The surface was patterned with laser parameters: λ = 1026 nm, 200 kHz and Δτ = 170 fs, while the laser beam polarization was horizontal.

Overall, an average of Λ_{HSFL} ~ 200 nm can be deduced and this constancy on periodicity of HSFL structures can be further seen in Fig. 22, where F_0 ranges from F_0 = 0.26 J/cm^2 to F_0 = 0.50 J/cm^2.

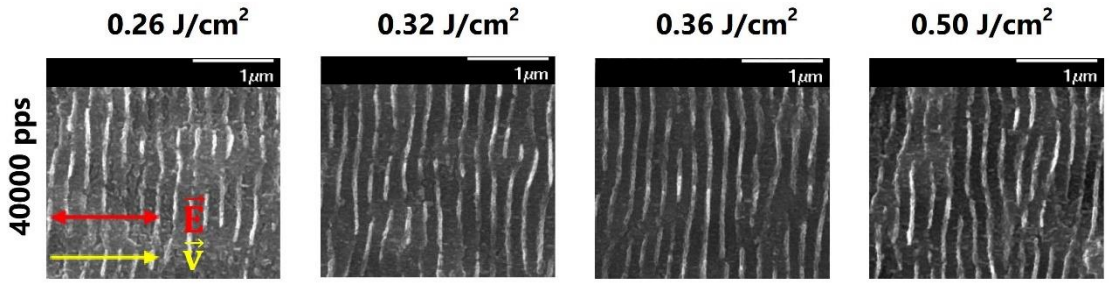

Figure 22. SEM images that indicate HSFL of constant period patterned on silicon surface with N_{eff} = 40000 pps and varying F_0. The surface was patterned with laser parameters: λ = 1026 nm, 200 kHz and Δτ = 170 fs, while red double-ended and yellow arrows indicate the beam polarization and scanning direction, respectively.

According to previous reports[5], [30], [31], for semiconductors, HSFL initiation, formation and arrangement at this high repetition rate femtosecond laser pulses combine modification of the surface initiated by heat accumulation of successive pulses with second harmonic generation (SHG), whereas as concluded in other reports[32], under the effect of SHG, the LSFL formed firstly with less pulses per spot seem to split and after all, the formation of HSFL perpendicular to initial laser polarization is evident. We could assume a combination of these theories and hence, a periodicity of $\Lambda_{HSFL} \sim \lambda/4$, is predicted roughly from SEM images.

4.1.2. Periodicity of HSFL as a function of effective number of pulses

On the other hand, HSFL have, also, been obtained by increasing the number of effective pulses per spot in a range of N_{eff} = 5000 pps to N_{eff} = 80000 pps as depicted in Fig. 20a. As illustrated in Fig. 23, for different constant values of peak laser fluence there is a general trend for the spacing of HSFL to decrease as N_{eff} increases up to a specific value and after that to remain constant as N_{eff} further increases up to 80000 pps. For example, for F_0 = 0.26 J/cm^2, Λ_{HSFL} = (236±37) nm when N_{eff} = 5000 pps, then decreases to Λ_{HSFL} = (185±25) nm when N_{eff} = 20000 pps and remains approximately constant to this value with further increase of N_{eff} up to 60000 pps.

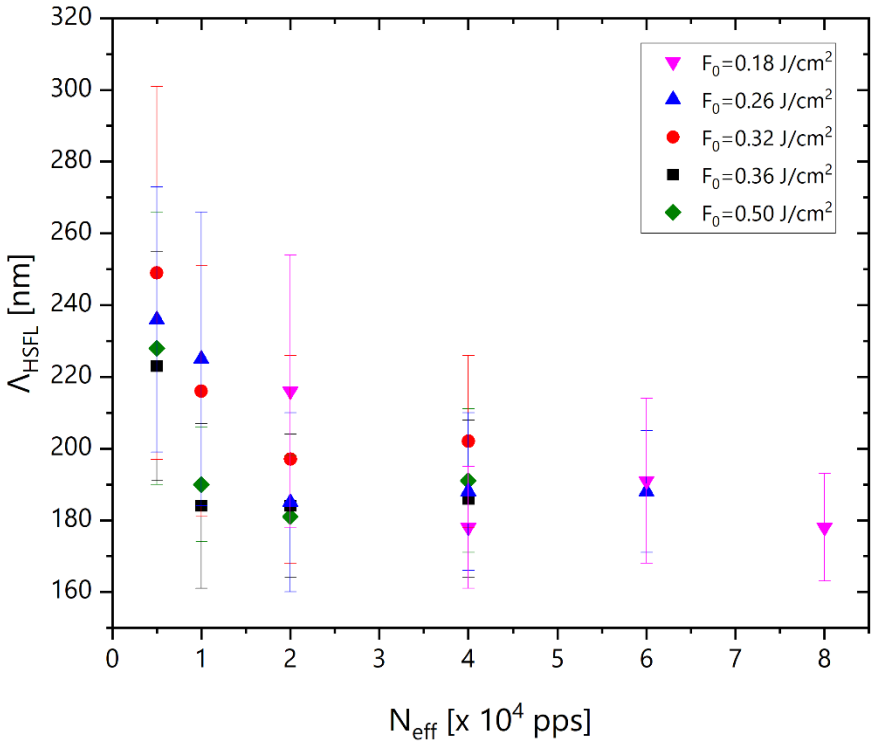

Figure 23. Periodicity of HSFL on silicon as a function of effective number of pulses per spot, N_{eff}. The surface was patterned with laser parameters: λ = 1026 nm, 200 kHz and Δτ = 170 fs, while the laser beam polarization was horizontal.

This drop on Λ_{HSFL}, for these particular irradiating conditions, can also be seen in SEM images of Fig. 24.

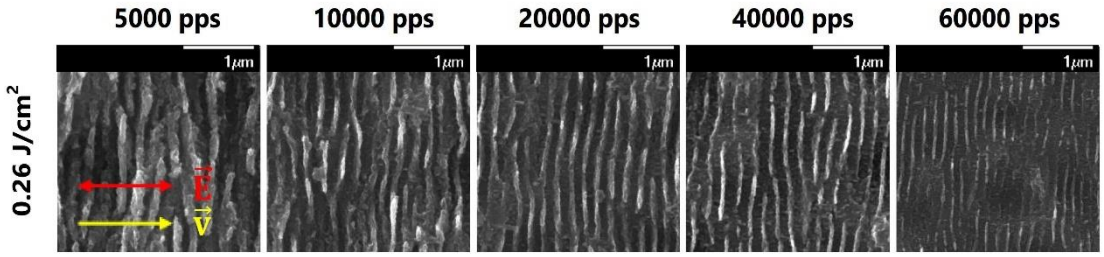

Figure 24. SEM images of silicon fabricated surface, that indicate HSFL spacing decreases as F_0 = 0.26 J/cm^2 is constant, while N_{eff} increases. The surface was patterned with laser parameters: λ = 1026 nm, 200 kHz and Δτ = 170 fs, while red double-ended and yellow arrows indicate the beam polarization and scanning direction, respectively.

Such a trend could be attributed to interference of the incident laser beam with near-field surface scattering, due to the presence of initial roughness on the irradiated surface.

A similar theory is accepted for the formation of LSFL-I in metals and, under specific conditions of irradiation, in semiconductors[11], as was discussed in the section with the proposed theoretical models for the formation of LIPSS. The origin of the aforementioned type of LSFL is connected to SPP excitation and interference with the incident irradiation, which successively leads to a periodic, grating-like, near-wavelength modulation of the radiated surface. Furthermore, as the effective number of pulses increases and as successive pulses irradiate the material, there is a blueshift of the plasmon-grating resonant frequency to smaller SPP wavelengths, because the surface grating profile becomes deeper.[18] Hence, in an equivalent way, and since the formation of both LSFL and HSFL can be attributed to interference of incident light with surface scattered waves, an analogous behavior could be expected for the evolution of periodicity of HSFL as the effective number of pulses per spot increases.

4.1.3. Height of HSFL

Finally, the height of HSFL ripples, h_{HSFL}, was measured via AFM images, as afore mentioned, and the estimation predicted that $h_{HSFL} \sim$ 200 nm. Hence, on silicon the periodical patterned topography can be classified as HSFL-I, since within the accepted error range, the depth-to-period aspect ratio is A > 1. In Fig. 25, a 3D image of modified silicon surface is presented, that was retrieved after scanning an (3 × 3) μm^2 area, which was fabricated with F_0 = 0.32 J/cm^2 and N_{eff} = 40000 pps.

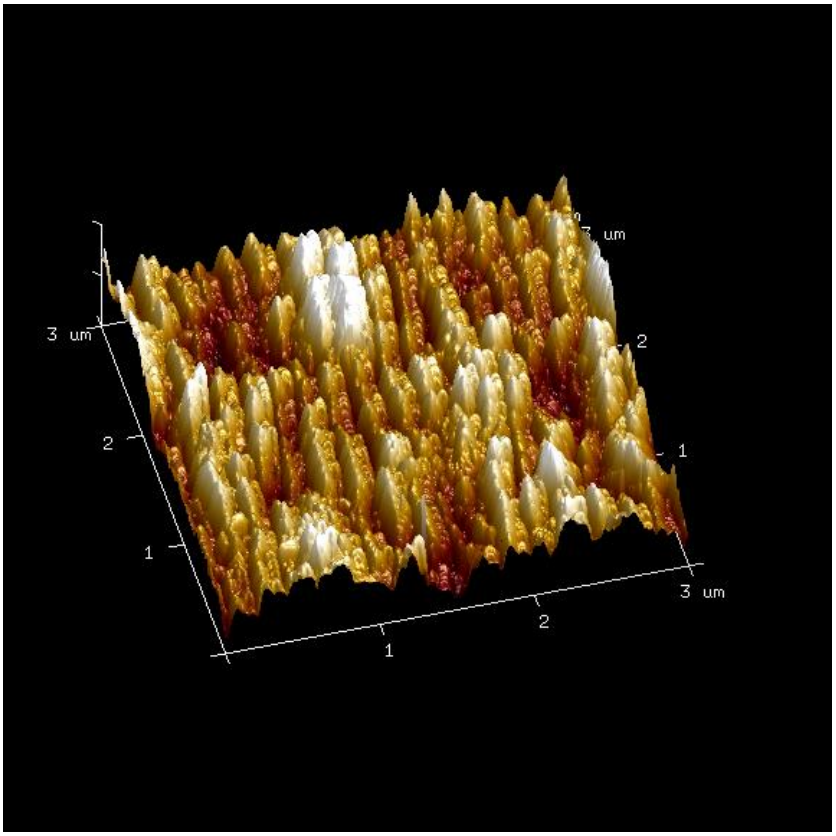

Figure 25. AFM image of silicon modified surface processed with F_0 = 0.32 J/cm^2, N_{eff} = 40000 pps, λ = 1026 nm, 200 kHz and Δτ = 170 fs, while the laser linear polarization was horizontal.

4.2. Nickel

For bulk nickel, the parametric study was conducted for N_{eff} ranging from N_{eff} = 5 pps (8.950 mm/s) to N_{eff} = 35 pps (1.279 mm/s) and for F_0 varying in a range from F_0 = 0.06 J/cm^2 to F_0 = 0.30 J/cm^2. These ranges were selected, as HSFL formation on metals initiates with small values of peak fluence.[33] Furthermore, as was the case in silicon, extended ranges of both N_{eff} and F_0, were chosen to be investigated in order to observe the transitions of induced morphologies on the surface topography. Fig. 26 depicts a map of the morphologies imprinted on the surface of bulk nickel and some characteristic corresponding SEM images for each value of both N_{eff} and F_0. As is illustrated, a variety of patterns -roughness, HSFL + roughness, HSFL, HSFL + LSFL and LSFL- are fabricated on nickel surface.

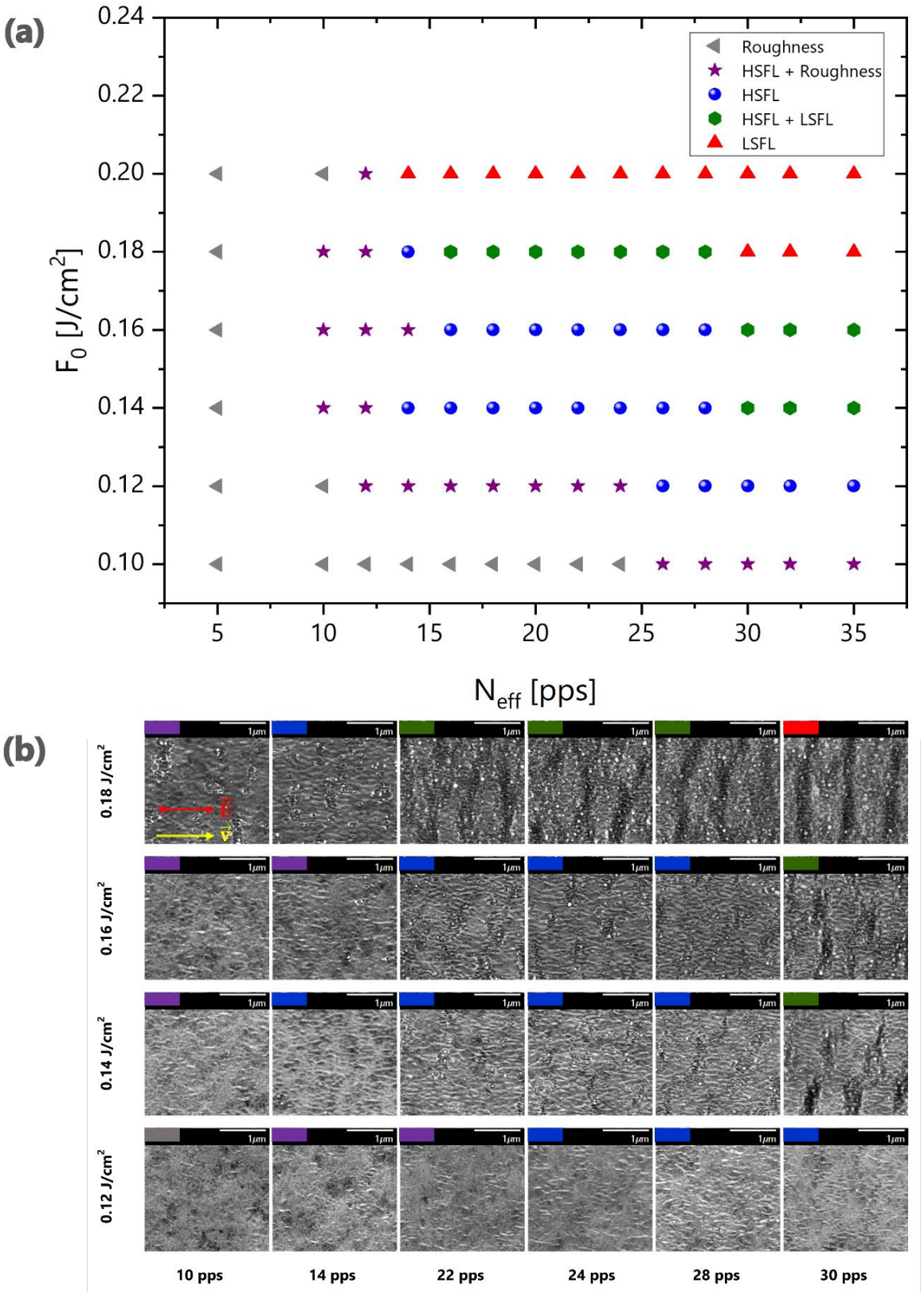

Figure 26. Map of the morphologies fabricated on nickel by linearly polarized beam scanning the irradiated surface with λ = 1026 nm, 1 kHz and Δτ = 170 fs. (a) Morphological map of nickel surface as a function of N_{eff} and F_0. (b) SEM images of the corresponding morphologies. Red double-ended and yellow arrows in (b) indicate the direction of laser polarization and of scanning velocity, respectively. The color of boxes on the top-left side of each image in (b) corresponds to coloration of structures in (a).

Particularly, for small values of N_{eff}, that is N_{eff} = 5 pps, only roughness is patterned on nickel surface for all values of F_0. By increasing N_{eff} and F_0, ripples start to form on the surface, starting from HSFL in combination with roughness, to HSFL, then to HSFL and LSFL and concluding to LSFL for the greatest N_{eff} and F_0. Combination of micro- and nano-structures is assumed in some cases, because the surface is not homogeneously and entirely covered with a specific type of ripples. Furthermore, since more pronounced HSFL seem to form along perpendicular ridges separated by distances equal to LSFL periods[33], the periodicity of HSFL is only measured on the ridges of many LSFL and not on the entire area, as was the case for silicon. Images were analyzed in this manner, because within the spacing of LSFL nonuniform HSFL-like structures with smaller periodicities are patterned. These nonuniform ripples with smaller periodicities form probably due to generation of secondary waves, that originate from debris near the edges of LSFL. These debris are shown in Fig. 27, along with some indicating areas, where the periodicity of HSFL, due to previously mentioned considerations, was measured. After all, the periodicity of HSFL under each irradiation condition, was statistically retrieved by averaging over the periodicities measured for each propriate area like the ones marked in green dashed boxes in Fig. 27.

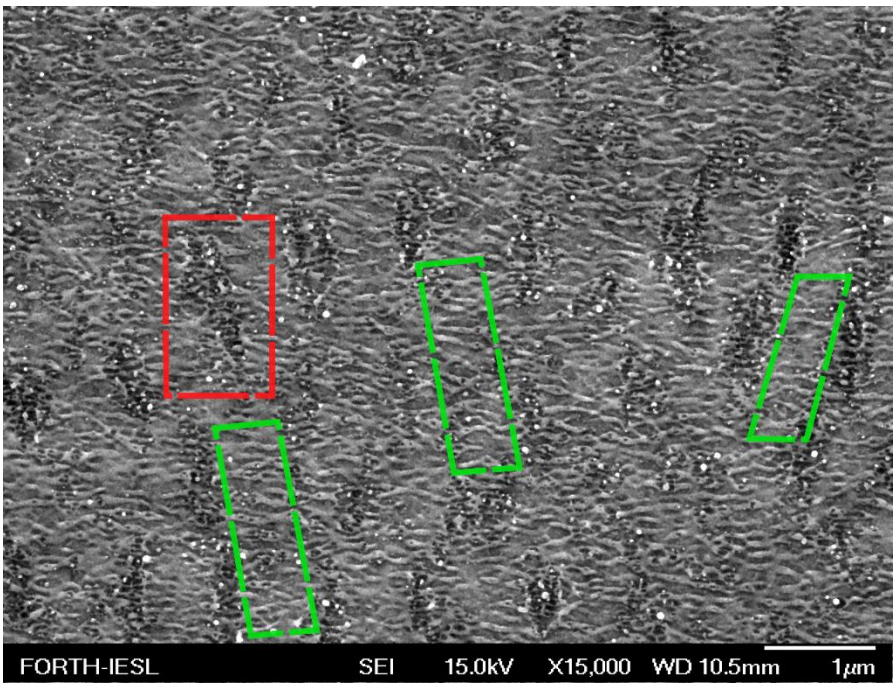

Figure 27. SEM image of nickel surface with F_0= 0.16 J/cm^2, N_{eff} = 22 pps, λ = 1026 nm, 1 kHz and Δτ = 170 fs. The laser polarization is horizontal. Red dashed box indicates an area with debris, that induce nonuniform HSFL-like structures with periodicities smaller than the periodicity of uniform HSFL on the ridges of LSFL and, thus such areas are excluded of Λ_{HSFL} measurements. Green dashed boxes indicate areas which HSFL cover homogeneously the irradiated surface, and hence accounting for average Λ_{HSFL}.

In the case of nickel, the orientation of HSFL is found to be parallel to laser polarization, regardless of F_0, N_{eff} and scanning direction. In order to estimate the HSFL periodicity, 2D-FFT analysis on selected areas of SEM images, as described above, was employed and the corresponding value was successfully verified via calculations of data retrieved from AFM images. Finally, the height of these periodical nanostructures was measured again via AFM images.

4.2.1. Periodicity of HSFL as a function of laser peak fluence

As is depicted on the map of Fig. 26a, there is a transient change from LSFL to HSFL as the laser peak fluence decreases. Specifically, HSFL that cover more homogeneously the entire surface of nickel are only formed for a narrow window of F_0, ranging from F_0 = 0.12 J/cm^2 to F_0 = 0.18 J/cm^2. Below this lower limit of F_0, roughness is formed on the irradiated surface, while for values of F_0 exceeding the upper limit for the formation of HSFL, the topography of the surface transiently changes, and LSFL start to form.

In Fig. 28, the dependence of periodicity of HSFL on laser peak fluence is illustrated. As can be deduced, for a constant effective number of pulses per spot, the spacing of periodic ripples is getting wider. Similar tendency to increase, or a constant value of Λ_{HSFL} with increasing F_0, is evident for the most conditions under investigation. In Fig. 29, SEM images are presented for this drop in periodicity, as F_0 reduces, to be evident.

Such a trend could be attributed to interference of the incident laser beam with near-field surface scattered waves, due to initial corrugation on the irradiated surface.

A similar behavior for the periodicity of LSFL-I is expected, that are formed due to interference of SPPs with incident radiation. The more energy that is periodically deposited to irradiated surface, the more carriers gain sufficient energy to be excited in higher energy levels in conduction band and hence, contribute as to decrease the refractive index. According to Drude model, refractive index reduces as the number of free carriers increases and thus, leads to an increase of SPPs periodicity, Λ_{SPP}. Λ_{SPP} is proportional to LSFL periodicity, as is indicated from equation (3), and correspondingly increases. [18], [19], [34] Thus, in an analogous way, and since the formation of both LSFL and HSFL seems to originate from interference of incident light with surface scattered electromagnetic waves, a similar behavior could be expected for the evolution of periodicity of HSFL as the laser peak fluence increases.

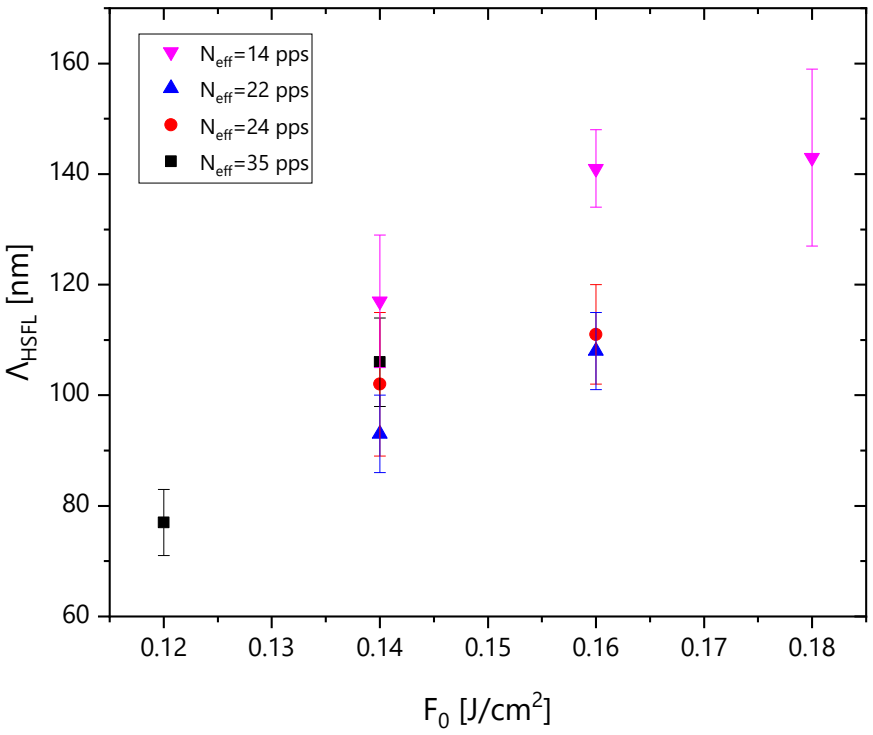

Figure 28. Periodicity of HSFL on nickel as a function of laser peak fluence, F_0. The surface was patterned with laser parameters: λ = 1026 nm, 1 kHz and Δτ = 170 fs, while the laser beam polarization was horizontal.

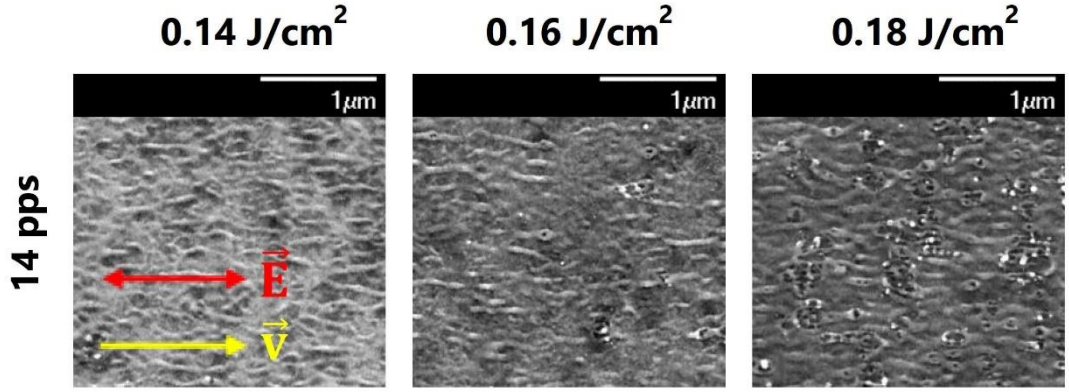

Figure 29. SEM images that indicate the increase in periodicity of HSFL on nickel as F_0 increases and N_{eff} = 14 pps is constant. The surface was patterned with laser parameters: λ = 1026 nm, 1 kHz and Δτ = 170 fs, while red double-ended and yellow arrows indicate the beam polarization and scanning direction, respectively.

4.2.2. Periodicity of HSFL as a function of effective number of pulses

As shown on the map of Fig. 26a, HSFL are again formed for a narrow range of effective number of pulses per spot. For N_{eff} < 14 pps (3.196 mm/s), roughness is formed, while for N_{eff} > 28 pps (1.598 mm/s) LSFL ripples are predominantly fabricated. Within the range of N_{eff} = 14 pps to N_{eff} = 28 pps, HSFL are patterned on the irradiated surface.

According to Fig. 30, as the effective number of pulses per spot increases, the periodicity of HSFL tends to decrease, as was the case for silicon.

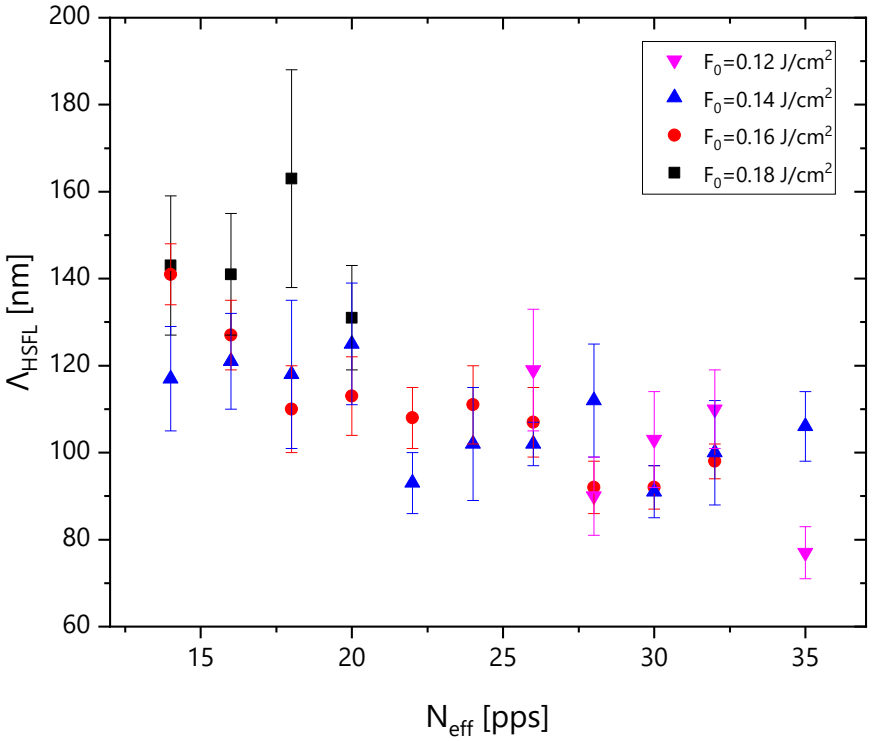

Figure 30. Periodicity of HSFL on nickel as a function of effective number of pulses per spot, N_{eff}. The surface was patterned with laser parameters: λ = 1026 nm, 1 kHz and Δτ = 170 fs, while the laser beam polarization was horizontal.

Thus, the formation of HSFL on nickel surface could be attributed to interference of incident light with near-field surface scattered waves, that indicate similar properties as SPPs, and hence analogous behavior could be expected. As was inferred for SPPs when successive pulses irradiate the surface, deeper structures are formed and within the deeper wells, the irradiating energy is absorbed more efficiently, hence leading to displacement of the plasmon-grating resonant frequency to smaller SPP wavelengths.[18] Thus, as long as the periodicity of LSFL is proportional to the periodicity of SPPs, narrower spacings are expected

as the effective number of pulses per spot is increased. In Fig. 31, this trend of Λ_{HSFL} to decrease as N_{eff} increases, while F_0 is constant, is illustrated.

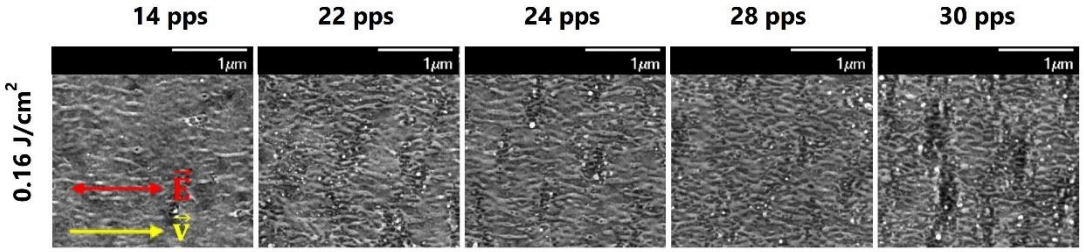

Figure 31. SEM images of nickel fabricated surface, that indicate HSFL spacing decreases as F_0 = 0.16 J/cm^2 is constant, while N_{eff} increases. The surface was patterned with laser parameters: λ = 1026 nm, 1 kHz and Δτ = 170 fs, while red double-ended and yellow arrows indicate the beam polarization and scanning direction, respectively.

4.2.3. Height of HSFL

Finally, the height of HSFL structures, h_{HSFL}, was also measured via AFM images and it was calculated h_{HSFL} ~ 15 nm. Hence, on nickel the induced periodical structures can be classified as HSFL-II, since their depth-to-period aspect ratio is A ~ 0.1 < 1.

In Fig. 32, a 3D image of nickel patterned surface is presented, that was retrieved after scanning an (1.5 × 1.5) μm^2 area, which was fabricated with F_0 = 0.16 J/cm^2 and N_{eff} = 24 pps.

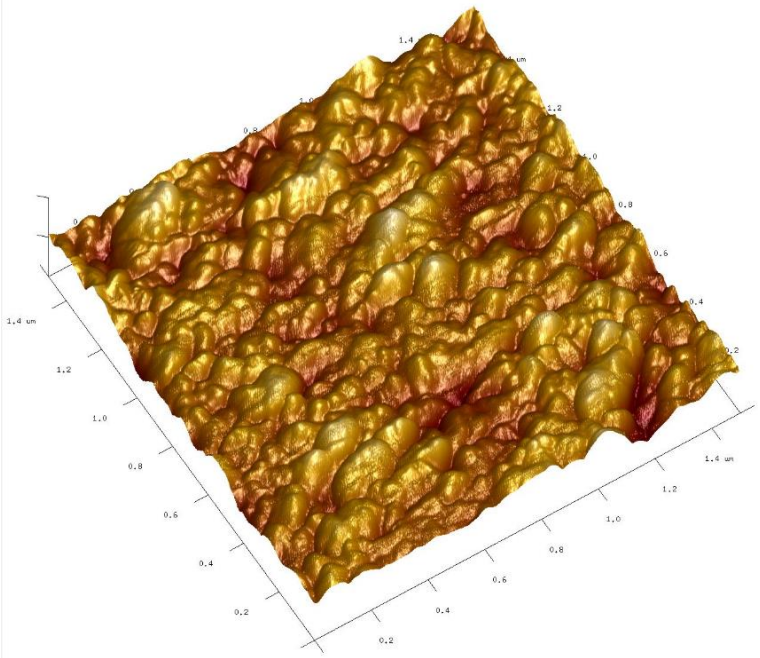

Figure 32. AFM image of nickel modified surface processed with F_0 = 0.16 J/cm^2, N_{eff} = 24 pps, λ = 1026 nm, 1 kHz and Δτ = 170 fs, while the laser linear polarization was horizontal.

4.3. Molybdenum

Molybdenum was chosen to be studied, as it possesses a great electron-phonon coupling factor and hence, very uniform LIPSS are to be expected to be formed. Again, since it is also a metal, HSFL are expected to start forming within small values of peak laser fluence. Furthermore, somewhat extended ranges of both N_{eff} and F_0, were considered in order to observe the transitions of induced morphologies on the surface topography. So, for bulk molybdenum, the parametric study was conducted for N_{eff} ranging from N_{eff} = 6 pps (98.750 mm/s) to N_{eff} = 1000 pps (0.593 mm/s) and for F_0 varying in a range from F_0 = 0.16 J/cm^2 to F_0 = 0.50 J/cm^2. Fig. 33 shows a map of the morphologies imprinted on the surface of molybdenum and some characteristic corresponding SEM images for each value of both N_{eff} and F_0. As is depicted, nonuniform HSFL, HSFL + LSFL (Ladder-like structures) and LSFL are patterned on the surface of bulk molybdenum.

Particularly, for small values of both N_{eff}, varying from N_{eff} = 6 pps to N_{eff} = 20 pps (29.625 mm/s), and F_0, varying from F_0 = 0.18 J/cm^2 to F_0 = 0.40 J/cm^2, only nonuniform HSFL were patterned on molybdenum surface. By increasing N_{eff}, up to N_{eff} = 60 pps (9.875 mm/s), ladder-like structures were formed for peak fluences ranging from F_0 = 0.18 J/cm^2 to F_0 = 0.40 J/cm^2. That is, vertical, pronounced and uniform LSFL ripples are dominant on the surface, but within their spacings horizontal HSFL are structured. Thus, the so-called ladder-like patterns. Similar modifications were also reported in the work of Taher et. al, on the irradiated surface of stainless-steel (304 AISI).[35] However, with further increasing of N_{eff}, HSFL disappeared and only LSFL were fabricated. Finally, when peak fluence was increased beyond F_0 = 0.40 J/cm^2, for all N_{eff} values studied, only LSFL were patterned on the surface of molybdenum.

Since horizontal HSFL were patterned for all irradiating conditions within the edges of LSFL, only specific areas, that were covered by HSFL, were assumed to contribute for the extraction of results for Λ_{HSFL}. In Fig. 34, these areas are marked in green dashed boxes. The periodicity of HSFL for each irradiating condition was calculated as the average of HSFL periodicities imprinted on each area and the uncertainty was calculated with standard deviation formula.

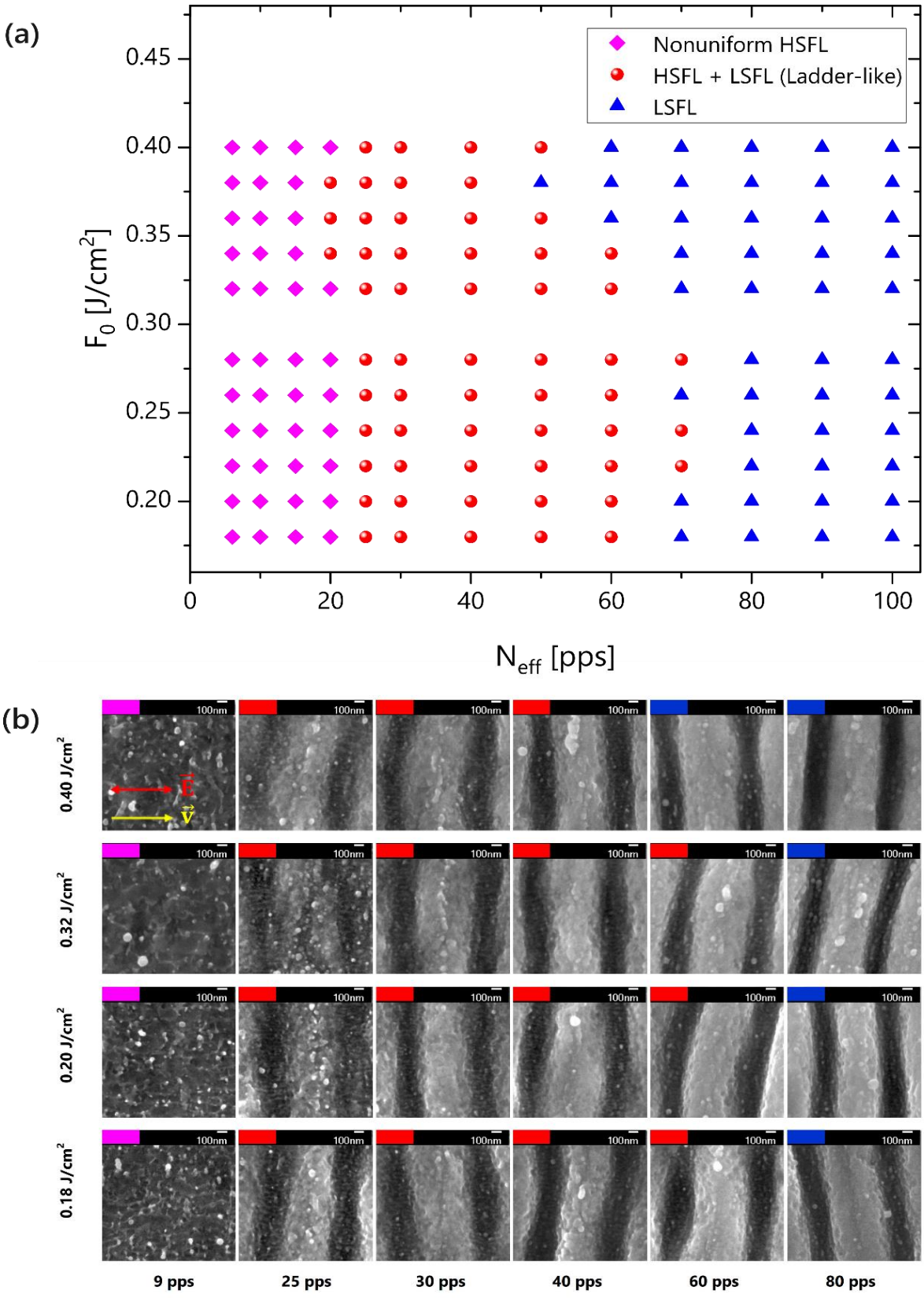

Figure 33. Map of the morphologies on molybdenum by linearly polarized beam scanning the irradiated surface with λ = 1030 nm, 10 kHz and Δτ = 350 fs. (a) Morphological map of molybdenum surface as a function of N_{eff} and F_0. (b) SEM images of the corresponding morphologies. Red double-ended and yellow arrows in (b) indicate the direction of laser polarization and of scanning velocity, respectively. The color of boxes on the top-left side of each image in (b) corresponds to coloration of structures in (a).

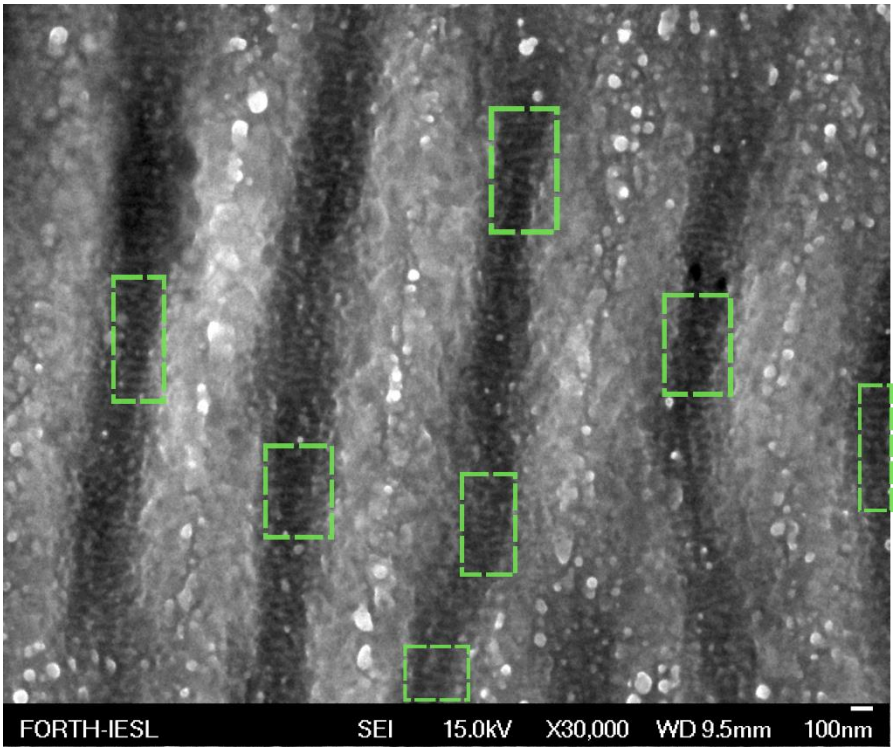

Figure 34. SEM image of molybdenum irradiated surface with F_0= 0.22 J/cm^2, N_{eff} = 30 pps, λ = 1030 nm, 10 kHz and Δτ = 350 fs. The laser polarization is horizontal. Green dashed boxes indicate areas which were taken into account to evaluate HSFL average periodicity, Λ_{HSFL}.

The fact that HSFL could not be observed alone, without the presence of dominant LSFL should be attributed to ~ 10 nm roughness of laser unprocessed molybdenum. This corrugation was probably carved due to mechanical polishing of the substrate and was estimated via AFM measurements.

However, the HSFL periodicity was predicted with 2D-FFT analysis on selected areas of SEM images, as described above. Although AFM measurements were employed to confirm the periodicities calculated via SEM images, the results retrieved were not reliable for HSFL structures, since only LSFL could be depicted. Furthermore, to account for the height of HSFL, AFM results were again not valid, as these periodical ripples are much shorter than LSFL. Finally, a 3D image of the modified surface will be provided to validate these considerations. It should be noted, that only observations for variation of Λ_{HSFL} as F_0 and N_{eff} change, are considered in these sub-sections, since HSFL were not obtained without the presence of LSFL.

4.3.1. Periodicity of HSFL as a function of laser peak fluence

As is evident in Fig. 33, HSFL within the spacing of LSFL are fabricated for peak fluence values ranging from F_0 = 0.18 J/cm^2 to F_0 = 0.40 J/cm^2, for N_{eff} ranging

from roughly N_{eff} = 20 pps to N_{eff} = 60 pps. In Fig. 35, the variation of Λ_{HSFL} with respect to F_0 is illustrated, for constant values of N_{eff}.

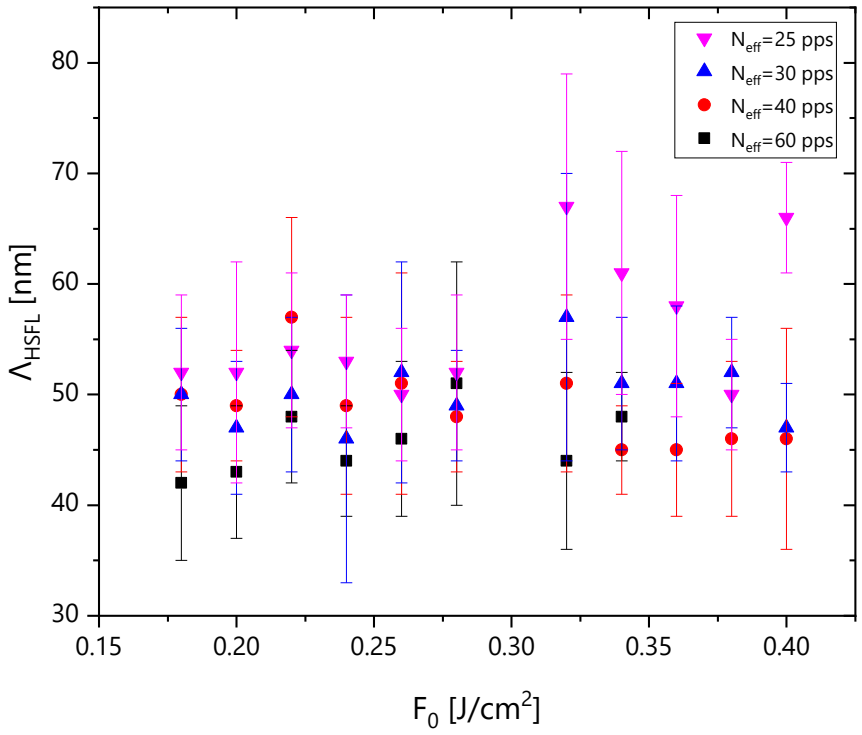

Figure 35. Periodicity of HSFL on molybdenum as a function of laser peak fluence, F_0. The surface was patterned with laser parameters: λ = 1030 nm, 10 kHz and Δτ = 350 fs, while the laser beam polarization was horizontal.

From Fig. 35, it can be deduced that the periodicity of HSFL is roughly constant, with no significant fluctuations, after all irradiating conditions. An average of $\Lambda_{HSFL} \sim 50$ nm can be estimated, implying that HSFL periodicity does not depend on laser peak fluence when the conditions of irradiation are such, that to allow for HSFL formation. After all, from periodic structures with spacing ~ λ/20 are induced on the irradiated surface of molybdenum substrate.

4.3.2. Periodicity of HSFL as a function of effective number of pulses

A plot of the periodicities attained, for irradiating conditions such that allowed for HSFL formation within the ridges of LSFL, along with their variation as the effecting number of pulses increase is represented in Fig. 36. As is evident from this diagram, there is a drop on Λ_{HSFL} as N_{eff} increases. This behavior is similar to the cases of silicon and nickel, for which the formation of HSFL was attributed to interference of near-field surface scattered waves with the incident laser light and second harmonic generation. Possibly these formation mechanisms could hold for the case of irradiated molybdenum substrate. However, since HSFL

were not obtained to form independently of LSFL, no reliable considerations can be made for the origin of these periodic nanoripples in the modified surface.

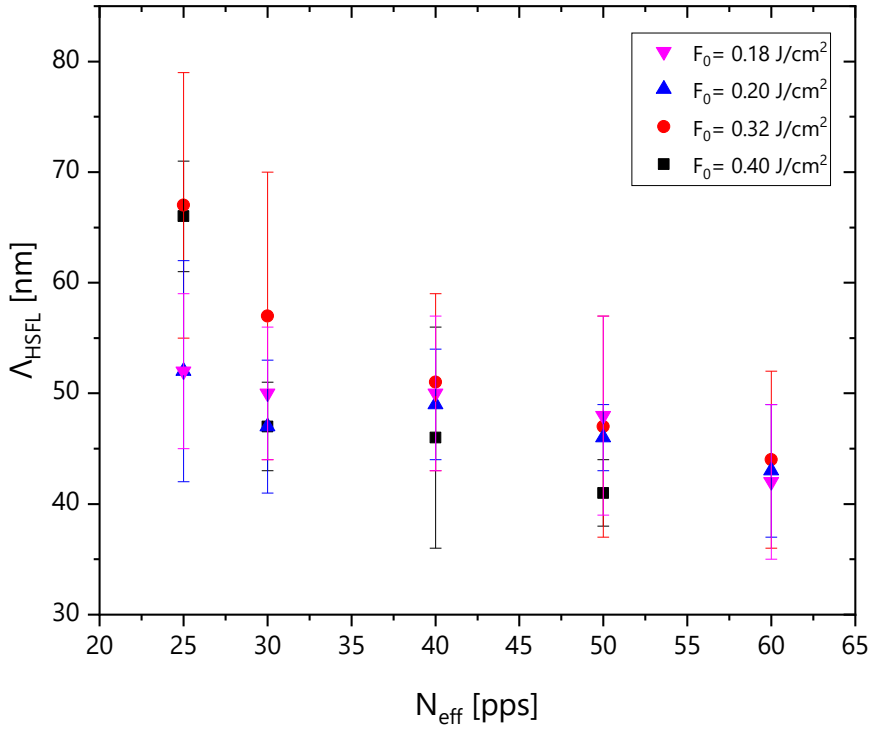

Figure 36. Periodicity of HSFL on molybdenum as a function of effective number of pulses per spot, N_{eff}. The surface was patterned with laser parameters: λ = 1030 nm, 10 kHz and Δτ = 350 fs, while the laser beam polarization was horizontal.

4.3.3. Height of HSFL

Finally, in Fig. 37 a 3D schematic of the topography of the irradiated molybdenum sample is provided, that was attained via AFM measurements. Due to presence of LSFL structures of height ~ 180 nm, no data could be derived for the height of HSFL, as it would be expected that they possess heights of ~ 10 nm. Nevertheless, this image is provided for the sake of completeness.

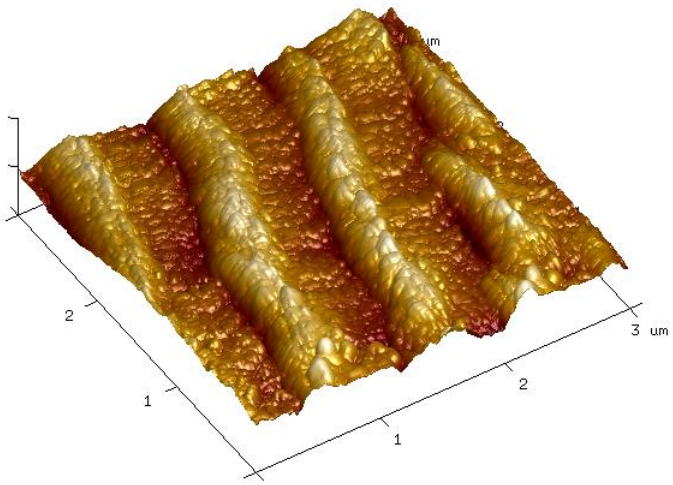

Figure 37. AFM image of molybdenum modified surface processed with F_0 = 0.28 J/cm^2, N_{eff} = 40 pps, λ = 1030 nm, 10 kHz and Δτ = 350 fs, while the laser linear polarization was horizontal.

5. Conclusions

To sum up, there are many conclusions that can be extracted throughout the analysis of accumulated experimental data and the results presented in this thesis. First of all, it is concluded that semiconductors and metals interact in different ways with electromagnetic radiation. As it was presented, HSFL perpendicular to laser polarization were formed on the surface of silicon, which is a semiconducting material, whereas in nickel and molybdenum, which are metals, HSFL ripples were parallel to laser polarization. Furthermore, in silicon uniform and homogeneous HSFL were patterned due to splitting of LSFL. By that, it can be deduced that some portion of the energy dose that irradiates the semiconductor surface is firstly consumed to change the material into plasmonically active, and after that acts destructively to further split the induced LSFL structures. This is also evident, by noticing the range of F_0 and N_{eff} allowing for HSFL formation. In the case of silicon, HSFL were attained for F_0 varying from F_0 = 0.16 J/cm^2 to F_0 = 0.80 J/cm^2 and for N_{eff} = 5000 pps to N_{eff} = 80000 pps. On the contrary, for nickel substrate this window was very narrow and HSFL were patterned for small values of N_{eff}, that is 35 pps - 14 pps, and F_0, 0.12 J/cm^2 – 0.18 J/cm^2. Also in molybdenum, although not solely observed, HSFL formation was achieved for laser peak fluence ranging from F_0 = 0.18 J/cm^2 to F_0 = 0.40 J/cm^2, and for effective number of pulses per spot ranging from N_{eff} = 20 pps to N_{eff} = 70 pps. It should be noted, however, that these parameters need to be carefully selected, as each combination among them results in different periodicities of grating-like nanostructures.

Within the scope of this thesis, was also to propose for some possible mechanisms leading to HSFL formation. As was discussed in detail, the most prominent mechanism seems to be the interference of incident light with the near-field scattered surface waves. Second harmonic generation was also proposed to account for HSFL fabrication, since under extreme irradiating conditions, the properties of studied material are expected to change. Furthermore, as both HSFL and LSFL could be attributed to interference of incident radiation with surface scattered waves, it could be inferred that the evolution of their periodicity when successive pulses irradiate the modified surface would follow a trend similar to SPPs periodicity.

At last, even now that the evolution of science and technology has enabled laser nanostructuring of surfaces, that leads to enhanced functionalities, there are still many questions on laser-matter interaction, that need to be answered. Some reasonable extensions of these questions and possible suggestions for future studies could be whether it could be possible to fabricate very uniform

HSFL on irradiated surfaces in a controllable way and if such structures could be achieved with different polarization states of incident laser light, for example. Then, along with unified theoretical considerations, light will be shed on the probable mechanism that leads to HSFL formation. Such a knowledge could allow for even more extensive utilization of these optimized structures and hence, it would pave the way for more complex and sophisticated technological ideas.

6. Bibliography

[1] E. Stratakis *et al.*, "Laser engineering of biomimetic surfaces."

[2] J. Bonse, S. Hohm, S. V. Kirner, A. Rosenfeld, and J. Kruger, "Laser-Induced Periodic Surface Structures-A Scientific Evergreen," *IEEE Journal of Selected Topics in Quantum Electronics*, vol. 23, no. 3, pp. 109–123, May 2017, doi: 10.1109/JSTQE.2016.2614183.

[3] M. Birnbaum, "Semiconductor surface damage produced by Ruby lasers," *J Appl Phys*, vol. 36, no. 11, pp. 3688–3689, 1965, doi: 10.1063/1.1703071.

[4] J. Bonse and S. Gräf, "Maxwell Meets Marangoni—A Review of Theories on Laser-Induced Periodic Surface Structures," *Laser and Photonics Reviews*, vol. 14, no. 10. Wiley-VCH Verlag, Oct. 01, 2020. doi: 10.1002/lpor.202000215.

[5] R. Le Harzic *et al.*, "Large-area, uniform, high-spatial-frequency ripples generated on silicon using a nanojoule-femtosecond laser at high repetition rate," 2011.

[6] J. Bonse, "Quo vadis LIPSS?—recent and future trends on laser-induced periodic surface structures," *Nanomaterials*, vol. 10, no. 10, pp. 1–19, Oct. 2020, doi: 10.3390/nano10101950.

[7] S. K. Sundaram and E. Mazur, "Inducing and probing non-thermal transitions in semiconductors using femtosecond laser pulses," *Nature Materials*, vol. 1, no. 4. European Association for Cardio-Thoracic Surgery, pp. 217–224, 2002. doi: 10.1038/nmat767.

[8] D. C. Emmony, R. P. Howson, and L. J. Willis, "Laser mirror damage in germanium at 10.6 μm," *Appl Phys Lett*, vol. 23, no. 11, pp. 598–600, 1973, doi: 10.1063/1.1654761.

[9] J. E. Sipe, J. F. Young, J. S. Preston, and H. M. Van Driel, "Laser-induced periodic surface structure. I. Theory," 1983.

[10] G. D. Tsibidis and E. Stratakis, "Ionisation processes and laser induced periodic surface structures in dielectrics with mid-infrared femtosecond laser pulses," *Sci Rep*, vol. 10, no. 1, Dec. 2020, doi: 10.1038/s41598-020-65613-w.

[11] M. Huang, F. Zhao, Y. Cheng, N. Xu, and Z. Xu, "Origin of laser-induced near-subwavelength ripples: Interference between surface plasmons and

incident laser," *ACS Nano*, vol. 3, no. 12, pp. 4062–4070, Dec. 2009, doi: 10.1021/nn900654v.

[12] D. Dufft, A. Rosenfeld, S. K. Das, R. Grunwald, and J. Bonse, "Femtosecond laser-induced periodic surface structures revisited: A comparative study on ZnO," *J Appl Phys*, vol. 105, no. 3, 2009, doi: 10.1063/1.3074106.

[13] A. Rudenko, C. Mauclair, F. Garrelie, R. Stoian, and J. P. Colombier, "Light absorption by surface nanoholes and nanobumps," *Appl Surf Sci*, vol. 470, pp. 228–233, Mar. 2019, doi: 10.1016/j.apsusc.2018.11.111.

[14] G. D. Tsibidis, M. Barberoglou, P. A. Loukakos, E. Stratakis, and C. Fotakis, "Dynamics of ripple formation on silicon surfaces by ultrashort laser pulses in subablation conditions," *Phys Rev B Condens Matter Mater Phys*, vol. 86, no. 11, Sep. 2012, doi: 10.1103/PhysRevB.86.115316.

[15] J. Hohlfeld *et al.*, "Electron and lattice dynamics following optical excitation of metals," 2000. [Online]. Available: www.elsevier.nlrlocaterchemphys

[16] J. M. Pitarke, V. M. Silkin, E. V. Chulkov, and P. M. Echenique, "Theory of surface plasmons and surface-plasmon polaritons," *Reports on Progress in Physics*, vol. 70, no. 1, pp. 1–87, Jan. 2007, doi: 10.1088/0034-4885/70/1/R01.

[17] Z. Han *et al.*, "Near-field photonics: surface plasmon polaritons and localized surface plasmons Radiation guiding with surface plasmon polaritons Surface plasmon polaritons: physics and applications Engineering metallic nanostructures for plasmonics and nanophotonics Plasmonics: visit the past to know the future Semiconductor plasmonic nanolasers: current status and perspectives Near-field photonics: surface plasmon polaritons and localized surface plasmons," 2003. [Online]. Available: http://iopscience.iop.org/1464-4258/5/4/353

[18] A. Margiolakis, G. D. Tsibidis, K. M. Dani, and G. P. Tsironis, "Ultrafast dynamics and subwavelength periodic structure formation following irradiation of GaAs with femtosecond laser pulses," *Phys Rev B*, vol. 98, no. 22, Dec. 2018, doi: 10.1103/PhysRevB.98.224103.

[19] E. Petrakakis, G. D. Tsibidis, and E. Stratakis, "Modelling of the ultrafast dynamics and surface plasmon properties of silicon upon irradiation with mid-IR femtosecond laser pulses," *Phys Rev B*, vol. 99, no. 19, May 2019, doi: 10.1103/PhysRevB.99.195201.

[20] J. Bonse, J. Krüger, S. Höhm, and A. Rosenfeld, "Femtosecond laser-induced periodic surface structures."

[21] Boyd, Robert. (2003). Chapter 1. The Nonlinear Optical Susceptibility. 10.1016/B978-012121682-5/50002-X.

[22] J. Bonse, A. Rosenfeld, and J. Krüger, "On the role of surface plasmon polaritons in the formation of laser-induced periodic surface structures upon irradiation of silicon by femtosecond-laser pulses," *J Appl Phys*, vol. 106, no. 10, 2009, doi: 10.1063/1.3261734.

[23] Joseph, T.,Verdeyen. Laser_Electronics. 3rd ed. (1995). Pearson

[24] J. M. Liu, "Simple technique for measurements of pulsed Gaussian-beam spot sizes," 1982.

[25] E. Stratakis, A. Ranella, and C. Fotakis, "Biomimetic micro/nanostructured functional surfaces for microfluidic and tissue engineering applications," *Biomicrofluidics*, vol. 5, no. 1, 2011, doi: 10.1063/1.3553235.

[26] A. Y. Vorobyev and C. Guo, "Direct femtosecond laser surface nano/microstructuring and its applications," *Laser and Photonics Reviews*, vol. 7, no. 3. pp. 385–407, May 2013. doi: 10.1002/lpor.201200017.

[27] V. Zorba *et al.*, "Silicon electron emitters fabricated by ultraviolet laser pulses," *Appl Phys Lett*, vol. 88, no. 8, 2006, doi: 10.1063/1.2177653.

[28] K. Sokolowski-Tinten, J. Bialkowski, and D. Von Der Linde, "Ultrafast laser-induced order-disorder transitions in semiconductors."

[29] J. Bonse, S. Baudach, J. Krüger, W. Kautek, and M. Lenzner, "Femtosecond laser ablation of silicon-modification thresholds and morphology," *Appl Phys A Mater Sci Process*, vol. 74, no. 1, pp. 19–25, 2002, doi: 10.1007/s003390100893.

[30] R. Le Harzic, F. Stracke, and H. Zimmermann, "Formation mechanism of femtosecond laser-induced high spatial frequency ripples on semiconductors at low fluence and high repetition rate," *J Appl Phys*, vol. 113, no. 18, May 2013, doi: 10.1063/1.4803895.

[31] R. Le Harzic, D. Dörr, D. Sauer, F. Stracke, and H. Zimmermann, "Generation of high spatial frequency ripples on silicon under ultrashort laser pulses irradiation," *Appl Phys Lett*, vol. 98, no. 21, May 2011, doi: 10.1063/1.3593493.

[32] X. Xu, L. Cheng, X. Zhao, J. Wang, K. Tong, and H. Lv, "Formation and Evolution of Micro/Nano Periodic Ripples on 2205 Stainless Steel

Machined by Femtosecond Laser," *Micromachines (Basel)*, vol. 14, no. 2, Feb. 2023, doi: 10.3390/mi14020428.

[33] C. S. R. Nathala *et al.*, "Experimental study of fs-laser induced sub-100-nm periodic surface structures on titanium," *Opt Express*, vol. 23, no. 5, p. 5915, Mar. 2015, doi: 10.1364/oe.23.005915.

[34] G. D. Tsibidis, M. Barberoglou, P. A. Loukakos, E. Stratakis, and C. Fotakis, "Dynamics of ripple formation on silicon surfaces by ultrashort laser pulses in subablation conditions," *Phys Rev B Condens Matter Mater Phys*, vol. 86, no. 11, Sep. 2012, doi: 10.1103/PhysRevB.86.115316.

[35] M. A. Taher, N. Chaudhary, K. Thirunaukkarasu, V. K. Rajput, and S. R. G. Naraharisetty, "Controlled periodicities of ladder-like structures via femtosecond laser of wavelength from 400 nm to 2200 nm," *Surfaces and Interfaces*, vol. 28, Feb. 2022, doi: 10.1016/j.surfin.2021.101622.

[36] Tsibidis, G.D., Stratakis, E. (2023). Ultrafast Laser Biomimetic Micro-/Nanostructuring. In: Stoian, R., Bonse, J. (eds) Ultrafast Laser Nanostructuring. Springer Series in Optical Sciences, vol 239. Springer, Cham. https://doi.org/10.1007/978-3-031-14752-4_25

[37] J. Bonse and S. Gräf, "Ten open questions about laser-induced periodic surface structures," *Nanomaterials*, vol. 11, no. 12, Dec. 2021, doi: 10.3390/nano11123326.